Nonlinear Dyn (2021) 103:1393–1414
https://doi.org/10.1007/s11071-020-06121-4

ORIGINAL PAPER

Thermomechanical modeling of nonlinear internal hysteresis due to incomplete phase transformation in pseudoelastic shape memory alloys

Jun Wang · Xiaojun Gu · Yingjie Xu ·
Jihong Zhu · Weihong Zhang

Received: 12 May 2020 / Accepted: 28 November 2020 / Published online: 8 February 2021

Abstract This paper presents a thermomechanical model for pseudoelastic shape memory alloys (SMAs) accounting for internal hysteresis effect due to incomplete phase transformation. The model is developed within the finite-strain framework, wherein the deformation gradient is multiplicatively decomposed into thermal dilation, rigid body rotation, elastic and transformation parts. Helmholtz free energy density comprises three components: the reversible thermodynamic process, the irreversible thermodynamic process and the physical constraints of both. In order to capture the multiple internal hysteresis loops in SMA, two internal variables representing the transition points of the forward and reverse phase transformation, ϕ_s^f and ϕ_s^r, are introduced to describe the incomplete phase transformation process. Evolution equations of the internal variables are derived and linked to the phase transformation. Numerical implementation of the model features an Euler discretization and a cutting-plane algorithm. After validation of the model against the experimental data, numerical examples are presented, involving a SMA-based vibration system and a crack SMA specimen subjected to partial loading–unloading case. Simulation results well demonstrate the internal hysteresis and free vibration behavior of SMA.

Keywords Shape memory alloys · Internal hysteresis · Incomplete phase transformation · Constitutive model · Numerical implementation

1 Introduction

Shape memory alloys (SMAs) are a kind of smart materials that exhibit large reversible deformation under appropriate thermomechanical loadings, characterized by shape memory effect (SME) and pseudoelasticity (PE) [1–4]. Their thermomechanical response displays profound hysteresis effect during phase transformation. This hysteresis is physically attributed to the frictional slipping between austenite and martensite variants at microscopic scale, while highly influenced by the macroscopic loading conditions [5,6]. In engineering applications, SMAs are usually used as functional devices such as sensors [7–10], actuators [11–15] and dampers [16–19]. For the sake of structural stability and functional fatigue, most of them are designed to service in the process of incomplete phase transformation, which may give rise to complex internal hysteresis loops in their thermodynamic response [20,21]. For example, some SMA actuators are designed to gen-

---

J. Wang · X. Gu · J. Zhu (✉)
Unmanned System Research Institute, Northwestern Polytechnical University, Xi'an 710072, China
e-mail: jh.zhu@nwpu.edu.cn

J. Wang · X. Gu · Y. Xu · J. Zhu · W. Zhang
State IJR Center of Aerospace Design and Additive Manufacturing, Northwestern Polytechnical University, Xi'an 710072, China

Y. Xu · J. Zhu
Shaanxi Engineering Laboratory of Aerospace Structure Design and Application, Northwestern Polytechnical University, Xi'an 710072, China

erate repeated motions against the externally applied force. At different loading rates and amplitudes, such repeated loading–unloading cycles may result in internal hysteresis loops [22,23]. Therefore, the study on the internal hysteresis of SMA is of high importance from the perspective of engineering application.

Over the last decades, great efforts were made to investigate the internal hysteresis response in SMA. From experimental point of view, [24] examined the stress–strain–temperature hysteresis behavior in an Fe-Cr-Ni-Mn-Si polycrystalline SMA during thermomechanical cyclic loading and drew transformation start and finish lines in the stress–temperature plane. The internal hysteresis behavior exhibited strong dependence on stress and temperature range. [25] carried out isothermal tensile tests on polycrystalline NiTi SMAs and observed two distinct forward and reverse transformation lines, which represented the initiation and completion of the internal hysteresis loops. [26] experimentally investigated the internal hysteresis behavior of NiTi SMA under various loadings. The internal loops were highly affected by the loading–unloading path, especially under stress-controlled loadings. [6] revealed that the main hysteresis loop may be defined as the envelope of all internal hysteresis loops. In order to gain a better understanding on the nucleation and progress of the incomplete phase transformation, [27] performed uniaxial tensile tests on NiTi SMA subjected to various partial loading–unloading conditions. It was observed that the strain on internal hysteresis loops increased during unloading while decreased during reloading. [28] used a digital camera and a motion analysis microscopic to observe the stress-induced martensite transformation (SIMT) bands on the SMA specimen subjected to complex internal loops. The internal hysteresis loops on the pseudoelastic stress–strain curves were related to the spreading and shrinking of the SIMT bands on the specimen. [29] presented experimental results of the torsion responses of SMA wires under incomplete phase transformation, and the return point memory for different internal loops was investigated. The shape and size of internal loops showed great dependence on the phase transformation history. These contributions indicated that the internal hysteresis is related to the incomplete phase transformation in SMA, while the initiation, growth and completion of martensite phase transformation depend on the thermomechanical loading conditions.

Based on the experimental findings, a few constitutive models were proposed to describe the internal hysteresis response of SMA. [24] carried out a phenomenological analysis on internal hysteresis loops due to incomplete phase transformation, in which the phase transformation start conditions were assumed to be dependent on the extent of prior transformation. Lagoudas et al. [30,31] developed a constitutive model for the internal hysteresis response of polycrystalline SMAs under cyclic loading, by combination of "thermomechanical models" and "control hysteresis models." A "re-visited" phase transformation criterion was introduced to properly account for incomplete phase transformation. [32] studied internal hysteresis in SMAs by means of the following procedure: (i) the subdivision of the system into units; (ii) the assignment of a critical driving force for phase transformation to each units; (iii) the definition of the interaction between units; and (iv) the specification of the initial conditions and the external field. [33] extended the concept of phase interaction energy function and proposed a microscopic approach to describe the internal hysteresis in SMAs. Polycrystalline SMA was assumed to be composed of a large number of single crystal grains, and the hysteresis behavior in each grain was represented by the Preisach model. [34] proposed a so-called shift-skip model to consider the internal hysteresis loops in SMA. The core concept of the model is the polycrystalline SMA which is composed of infinite number of grains, and the martensite phase transformation takes place grain by grain. [35] constructed a constitutive model of SMAs within the Ziegler–Green–Naghdi framework, which is able to capture the internal hysteresis due to both incomplete phase transformation and martensite reorientation. [36] introduced a "dissipationless band" to model the internal hysteresis response in SMAs. It is assumed that the mechanical dissipation is proportional to the magnitude of the product phase formation. [37] employed the theory of thermally activated processes to describe the kinetics of phase transformations responsible for the hysteresis behavior in single crystal SMA and generalized it to polycrystalline SMAs by incorporating the concept of inhomogeneities and effective stresses. The internal hysteresis in polycrystalline SMAs was associated with the inhomogeneous phase transformation and the stress concentration at grain boundaries. [38] presented a thermodynamic argument to interpret the observed internal hysteresis in CuAlNi SMA in terms of interfacial energies. [29] presented a revised Preisach model to capture the complex internal loops in pseudoelastic SMAs by modeling the relationship between the driving force for phase transformation and the martensite volume fraction.

The aforementioned models show certain capabilities to address the internal hysteresis of SMA subjected to partial loading conditions. However, most of them have potential limitations. For example, the early one-dimensional model is limited to describe hysteresis curves from the phenomenological point of view [24]. The "single crystal to polycrystal" models normally have a tedious modeling procedure [32,37]. The "shift-skip" and "dissipationless band" models introduced some fictitious assumptions, such as the dissipationless or "grain-by-grain" martensite phase transformation [34,36]. The "Preisach-based" models consist of many relay hysterons connected in parallel, and the prediction precision is highly dependent on the number of hysterons used in the model [29,33]. In the model of [29], more than 20,000 hysterons were used to capture the internal hysteresis loops, while the stress–strain curve still shows jagged response. Besides, all of them were developed under assumption of infinitesimal strain, though the strain levels in internal hysteresis loops have definitely entered finite-strain regime. Last and most important, the recent representative SMA models were focused on either pseudoelasticity [2,39] or plasticity [4,40] upon complete phase transformation, but overlooked the complex internal hysteresis when SMAs undergo incomplete phase transformation.

To address the above concerns, this paper develops a new constitutive model, within a finite-strain and thermodynamically consistent framework, to describe the complex internal hysteresis in pseudoelastic SMA. It is organized as follows: Sect. 2 presents the kinematic hypothesis. Section 3 gives the Helmholtz free energy density. Section 4 discusses the thermodynamic consistency. Section 5 derives the constitutive equations. Section 6 details the numerical implementation procedure of the model. Section 7 validates the model against the experimental data. Section 8 studies the free vibration behavior of SMA. Section 9 provides a numerical example involving a crack SMA specimen. Finally, Section 10 draws a conclusion of this paper.

2 Kinematics

Consider a homogeneous body B that occupies an open region of the three-dimensional Euclidean space $\mathcal{B}$, the material particle in the body B is identified with $\boldsymbol{p}$. The motion of the body B within an open time interval t is a smooth one-to-one function $\boldsymbol{\varphi}$ that maps the material particle $\boldsymbol{p}$ to its spatial point $\boldsymbol{x}$ at time t. The deformation gradient of the motion $\boldsymbol{\varphi}$ is the second-order tensor $\boldsymbol{F}$, defined by

$$\boldsymbol{F} = \nabla_m \boldsymbol{\varphi} \quad \text{with} \quad J \equiv \det \boldsymbol{F} > 0 \quad \text{and} \quad F_{ij} = \frac{\partial x_i}{\partial p_j}, \tag{1}$$

where ∇_m denotes the material gradient of a general field, J denotes the determinant of $\boldsymbol{F}$, and F_{ij} are the Cartesian components of $\boldsymbol{F}$.

The velocity field $\boldsymbol{v}$ and the velocity gradient $\boldsymbol{L}$ of the motion $\boldsymbol{\varphi}$ are defined by

$$\boldsymbol{v} = \dot{\boldsymbol{\varphi}} \quad \text{and} \quad \boldsymbol{L} = \nabla_s \boldsymbol{v} = \dot{\boldsymbol{F}} \boldsymbol{F}^{-1}, \tag{2}$$

where $\dot{*}$ denotes the material time derivative of a general field $*$, and ∇_s denotes the spatial gradient of a general field. The symmetric and skew parts of $\boldsymbol{L}$ are referred to, respectively, as the stretching and spin tensors, given by

$$\boldsymbol{D} = \text{sym}(\boldsymbol{L}) = \frac{1}{2}(\boldsymbol{L} + \boldsymbol{L}^T) \quad \text{and}$$
$$\boldsymbol{W} = \text{skew}(\boldsymbol{L}) = \frac{1}{2}(\boldsymbol{L} - \boldsymbol{L}^T). \tag{3}$$

Generally, the existing SMA models using finite strain formulation are developed based on two kinematic assumptions: the additive split of the stretching tensor $\boldsymbol{D}$ [41–43] or the multiplicative decomposition of the deformation gradient $\boldsymbol{F}$ [44–46] into elastic and inelastic components. The former approach is expressed directly in rate form and would be consistent with the latter if appropriate integrability conditions are satisfied. Here, to model the internal hysteresis response of SMA due to incomplete phase transformation, we introduce a tripartite decomposition of the deformation gradient into elastic, phase transformation and thermal parts [47]

$$\boldsymbol{F} = \boldsymbol{F}^{\mathrm{e}} \boldsymbol{F}^{\mathrm{t}} \boldsymbol{F}^{\theta} \tag{4}$$

where $\boldsymbol{F}^{\mathrm{e}}$ is defined on a local stress-free intermediate configuration, $\boldsymbol{F}^{\mathrm{t}}$ is defined on a thermally dilated configuration, and $\boldsymbol{F}^{\theta}$ is defined on the reference configuration. With regard to the deformations, we make the following kinematic assumptions:

- For general inhomogeneous inelastic deformation, the stress-free intermediate configuration obtained by unloading a body is, in general, not uniquely determined since the superposition of an arbitrary rigid body rotation still leaves it at zero stress state. In order to overcome this uniqueness problem, all the rigid body rotation is separated from the elastic and transformation deformations, such that the elastic and transformation deformation gradients, $\boldsymbol{F}^{\mathrm{e}}$ and $\boldsymbol{F}^{\mathrm{t}}$, include only stretch tensors [48]. As a result, they are written

  $$\boldsymbol{F}^{\mathrm{e}} = \boldsymbol{V}^{\mathrm{e}} \quad \text{and} \quad \boldsymbol{F}^{\mathrm{t}} = \boldsymbol{V}^{\mathrm{t}}, \tag{5}$$

  where $\boldsymbol{V}^{\mathrm{e}}$ and $\boldsymbol{V}^{\mathrm{t}}$ are the symmetric stretch tensors.
- The polycrystalline SMAs are commonly considered as isotropic materials. In view of this, we assume (i) the thermal deformation is an isotropic thermal dilation, i.e., $\boldsymbol{F}^{\theta} = J^{\theta\frac{1}{3}}\mathbf{1}$; (ii) the transformation deformation is incompressible and irrotational (zero transformation spin) [49], i.e., $J^{\mathrm{t}} \equiv \det \boldsymbol{V}^{\mathrm{t}} = 1$ and $\boldsymbol{W}^{\mathrm{t}} = 0$.
- We split the elastic deformation gradient into volumetric and isochoric components, i.e., $\boldsymbol{V}^{\mathrm{e}} = J^{\mathrm{e}\frac{1}{3}}\bar{\boldsymbol{V}}^{\mathrm{e}}$. By combination of these assumptions, we then have the isochoric/volumetric split of the deformation gradient $\boldsymbol{F} = J^{\frac{1}{3}}\bar{\boldsymbol{F}}$, where $J = J^{\mathrm{e}}J^{\theta}$ denotes the pure volumetric component and $\bar{\boldsymbol{F}} = \bar{\boldsymbol{V}}^{\mathrm{e}}\boldsymbol{V}^{\mathrm{t}}$ denotes the pure isochoric component.

Using the above kinematic assumptions, the decomposition of the deformation gradient in Eq. (4) is written

$$\boldsymbol{F} = J^{\frac{1}{3}}\bar{\boldsymbol{V}}^{\mathrm{e}}\boldsymbol{V}^{\mathrm{t}}\boldsymbol{R}, \tag{6}$$

where $\boldsymbol{R}$ is a proper orthogonal tensor (local rotation) obtained by the polar decomposition of the deformation gradient $\boldsymbol{F} = \boldsymbol{V}\boldsymbol{R}$. Figure 1 schematically illustrates the four-tier decomposition in Eq. (6). For the material particle $\boldsymbol{p}$, it first undergoes an isotropic thermal dilation. Then, the local rotation tensor $\boldsymbol{R}$ rotates the reference configuration into a new configuration that includes all the rigid body motion. Subsequently, martensite transformation and reorientation take place on the intermediate stress-free configuration. Finally, martensite variants are distorted under elastic loading, and the material particle $\boldsymbol{p}$ gets to the spatial point $\boldsymbol{x}$.

The substitution of Eq. (6) into Eq. $(2)_2$ results in an additive split of the velocity gradient

$$\boldsymbol{L} = \bar{\boldsymbol{L}}^{\mathrm{e}} + \bar{\boldsymbol{V}}^{\mathrm{e}}\boldsymbol{L}^{\mathrm{t}}\bar{\boldsymbol{V}}^{e^{-1}} + \bar{\boldsymbol{V}}\boldsymbol{\Omega}\bar{\boldsymbol{V}}^{-1} + \frac{1}{3}\dot{\delta}\mathbf{1} \tag{7}$$

where $\bar{\boldsymbol{L}}^{\mathrm{e}} = \dot{\bar{\boldsymbol{V}}}^{\mathrm{e}}\bar{\boldsymbol{V}}^{e^{-1}}$ and $\boldsymbol{L}^{\mathrm{t}} = \dot{\boldsymbol{V}}^{\mathrm{t}}\boldsymbol{V}^{\mathrm{t}-1}$ denote, respectively, the elastic and transformation velocity gradients, $\boldsymbol{\Omega} = \dot{\boldsymbol{R}}\boldsymbol{R}^{\mathrm{t}}$ is a skew tensor representing the spin of the reference configuration, and $\delta = \ln J$ denotes the spherical component of the logarithmic strain tensor.

The Eulerian Hencky strain measures and their spectral decompositions are defined as

$$\begin{aligned}
\boldsymbol{h} &= \ln \boldsymbol{V} = \sum_{i=1}^{3} \ln \lambda_i \, \boldsymbol{e}_i \otimes \boldsymbol{e}_i \\
\bar{\boldsymbol{h}}^{\mathrm{e}} &= \ln \bar{\boldsymbol{V}}^{\mathrm{e}} = \sum_{i=1}^{3} \ln \bar{\lambda}_i^{\mathrm{e}} \, \boldsymbol{e}_i^{\mathrm{e}} \otimes \boldsymbol{e}_i^{\mathrm{e}} \\
\boldsymbol{h}^{\mathrm{t}} &= \ln \boldsymbol{V}^{\mathrm{t}} = \sum_{i=1}^{3} \ln \lambda_i^{\mathrm{t}} \, \boldsymbol{e}_i^{\mathrm{t}} \otimes \boldsymbol{e}_i^{\mathrm{t}}
\end{aligned} \tag{8}$$

where λ_i is the eigenvalue of $\boldsymbol{V}$ named principle stretch, and $\boldsymbol{e}_i$ is the eigenvector of $\boldsymbol{V}$. The trial $\{\boldsymbol{e}_1, \boldsymbol{e}_2, \boldsymbol{e}_3\}$ forms orthonormal bases for the tensor fields on the spatial configuration and defines the Eulerian principle directions of the stretches.

3 Helmholtz free energy

The Helmholtz free energy density ψ is assumed to depend on the following state variables:

- Spherical tensor of total logarithmic strain $\delta\mathbf{1}$.
- Deviatoric tensor of elastic Eulerian Hencky strain $\bar{\boldsymbol{h}}^{\mathrm{e}}$.
- Transformation Eulerian Hencky strain tensor $\boldsymbol{h}^{\mathrm{t}}$.
- Martensite volume fraction ϕ and absolute temperature θ.
- Transition point of forward phase transformation ϕ_s^f (A → M).

Fig. 1 Multiplicative decomposition of the deformation gradient according to the different deformation mechanisms

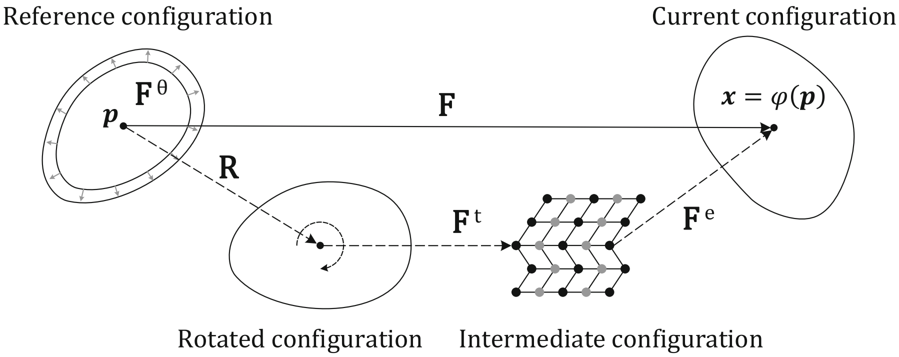

- Transition point of reverse phase transformation ϕ_s^r (M → A).

According to the thermodynamic mechanisms in SMA, we consider that the Helmholtz free energy density per unit volume on spatial configuration is additively decomposed into three components:

$$\psi(\delta, \bar{\boldsymbol{h}}^{\mathrm{e}}, \boldsymbol{h}^{\mathrm{t}}, \theta, \phi, \phi_s^f, \phi_s^r) = \psi^r(\delta, \bar{\boldsymbol{h}}^{\mathrm{e}}, \theta, \phi) + \psi^{ir}(\boldsymbol{h}^{\mathrm{t}}, \phi) + \psi^{pc}(\boldsymbol{h}^{\mathrm{t}}, \phi, \phi_s^f, \phi_s^r), \tag{9}$$

where ψ^r represents the reversible thermodynamic process, ψ^{ir} the irreversible thermodynamic process, and ψ^{pc} the physical constraints of the both processes.

The first component ψ^r includes two reversible thermodynamic processes: elastic deformation and temperature change, given as

$$\begin{aligned}\psi^r = &\underbrace{\frac{1}{2}K\delta^2 + \mu\sum_{i=1}^{3}(\bar{h}_i^{\mathrm{e}})^2 - 3\alpha K\delta(\theta - \theta_0)}_{\text{elastic deformation}}\\ &\underbrace{+\, e_0 - \eta_0\theta + \phi\Delta_\eta(\theta - \theta_0) + c\left[(\theta - \theta_0) - \theta\ln\left(\frac{\theta}{\theta_0}\right)\right]}_{\text{temperature change}},\end{aligned} \tag{10}$$

where K and μ are the bulk and shear moduli, $\bar{h}_i^{\mathrm{e}} = \ln\bar{\lambda}_i^{\mathrm{e}}$ is the eigenvalue of the elastic Eulerian Hencky strain, α is the thermal expansion coefficient, θ_0 is the reference temperature, e_0 and η_0 denote the internal energy and entropy at the reference temperature, Δ_η denotes the entropy difference between the austenite and martensite phases, and c is the specific heat capacity.

The second component ψ^{ir} refers to the free energy density due to the stress- or temperature-induced phase transformation, given as

$$\psi^{ir} = g^{\mathrm{t}}(\phi) + \frac{1}{2}\mu_t\sum_{i=1}^{3}(h_i^{\mathrm{t}})^2, \tag{11}$$

where the first term g^{t} represents the interface energy between austenite and martensite, the second term represents the energy increase due to martensite orientation/reorientation, μ_t denotes the hardening modulus of martensite phase transformation, and $h_i^{\mathrm{t}} = \ln\lambda_i^{\mathrm{t}}$ is the eigenvalue of the transformation Eulerian Hencky strain.

The last component ψ^{pc} is a Lagrangian potential, and we introduce it to guarantee the physical constraints that the state variables must obey, which is given as

$$\psi^{pc} = \mathcal{I}_{[0,1]}(\phi) + \mathcal{I}_{[0,\mathcal{H}]}(\boldsymbol{h}^{\mathrm{t}}) + \mathcal{I}_{(0,1)}(\phi_s^f, \phi_s^r), \tag{12}$$

where the first term $\mathcal{I}_{[0,1]}$ is set to enforce the physical constraint on ϕ as

$$\mathcal{I}_{[0,1]}(\phi) = \begin{cases} 0 & \text{if } \ 0 \le \phi \le 1 \\ +\infty & \text{otherwise} \end{cases} \tag{13}$$

the second term $\mathcal{I}_{[0,\mathcal{H}]}$ is set to enforce the physical constraint on $\boldsymbol{h}^{\mathrm{t}}$ as

$$\mathcal{I}_{[0,\mathcal{H}]}(\boldsymbol{h}^{\mathrm{t}}) = \begin{cases} 0 & \text{if } \ 0 \le \|\boldsymbol{h}^{\mathrm{t}}\| \le \mathcal{H} \\ +\infty & \text{otherwise} \end{cases} \tag{14}$$

the constant $\mathcal{H}$ denotes the saturation value of the martensite reorientation strain, and the last term $\mathcal{I}_{(0,1)}$ is set to enforce the physical constraint on ϕ_s^f and ϕ_s^r as

$$\mathcal{I}_{(0,1)}(\phi_s^f, \phi_s^r) = \begin{cases} 0 & \text{if } \ 0 < \phi_s^f, \phi_s^r < 1 \\ +\infty & \text{otherwise} \end{cases} \tag{15}$$

Here, it is noted that the Lagrangian potentials $\mathcal{I}_*$ in essence act as penalty functions, by which the state variables are confined within the constrained boundaries. The introduction of the Lagrangian potentials into the Helmholtz free energy turns constrained problem into unconstrained one and also guarantees differentiability of the free energy potential.

4 Consequences of thermodynamics

The principle of virtual power (PVP), the conservation of energy (first law of thermodynamics) and the irreversibility of entropy production (second law of thermodynamics) are the three most important fundamentals in continuum mechanics and development of constitutive theories. Recalling the body B being subjected to volume forces $\boldsymbol{T}_v$ in its interior and contact forces $\boldsymbol{T}_c$ on its boundary, its deformed (spatial) configuration occupies the region $\boldsymbol{\varphi}(\mathcal{B})$ with boundary $\boldsymbol{\varphi}(\partial\mathcal{B})$. The balance of momentum for B can be expressed in terms of the Cauchy stress tensor $\boldsymbol{\sigma}$ on the spatial configuration as

$$\begin{aligned} &\mathrm{div}_s\boldsymbol{\sigma} + \boldsymbol{T}_v = \rho\dot{\boldsymbol{v}} \quad \forall \boldsymbol{x} \in \boldsymbol{\varphi}(\mathcal{B}) \quad \text{and} \\ &\quad \boldsymbol{T}_c = \boldsymbol{\sigma}\boldsymbol{n} \quad \forall \boldsymbol{x} \in \boldsymbol{\varphi}(\partial\mathcal{B}) \end{aligned} \tag{16}$$

where div_s denotes the spatial divergence of a general field, and $\boldsymbol{n}$ denotes the outward unit vector normal to $\boldsymbol{\varphi}(\partial\mathcal{B})$. Equation (16) is often referred to as the strong equilibrium. Alternatively, the weak equilibrium (PVP) for the body B is formulated on the spatial configuration as

$$\begin{aligned} &\int_{\boldsymbol{\varphi}(\mathcal{B})} \left[\boldsymbol{\sigma} : \nabla_s \boldsymbol{\mathcal{V}}^* + (\rho\dot{\boldsymbol{v}} - \boldsymbol{T}_v)\cdot\boldsymbol{\mathcal{V}}^*\right] \mathrm{dV} \\ &\quad - \int_{\boldsymbol{\varphi}(\partial\mathcal{B})} \boldsymbol{T}_c \cdot \boldsymbol{\mathcal{V}}^* \,\mathrm{dS} = 0, \end{aligned} \tag{17}$$

where $\boldsymbol{\mathcal{V}}^*$ denotes an arbitrary virtual velocity field. Substitution of the real velocity field $\boldsymbol{v}$ and gradient $\boldsymbol{L}$ defined in Eq. (2) into Eq. (17) produces

$$\begin{aligned} &\underbrace{\int_{\boldsymbol{\varphi}(\mathcal{B})} \boldsymbol{\sigma} : \boldsymbol{L}\,\mathrm{dV}}_{\mathcal{P}_{it}} + \underbrace{\int_{\boldsymbol{\varphi}(\mathcal{B})} \rho\dot{\boldsymbol{v}}\cdot\boldsymbol{v}\,\mathrm{dV}}_{\mathcal{P}_a} \\ &\quad = \underbrace{\int_{\boldsymbol{\varphi}(\mathcal{B})} \boldsymbol{T}_v\cdot\boldsymbol{v}\,\mathrm{dV} + \int_{\boldsymbol{\varphi}(\partial\mathcal{B})} \boldsymbol{T}_c\cdot\boldsymbol{v}\,\mathrm{dS}}_{\mathcal{P}_{ext}}, \end{aligned} \tag{18}$$

where $\mathcal{P}_{it}$ denotes the internal stress power, $\mathcal{P}_a$ denotes the power of inertial forces, and $\mathcal{P}_{ext}$ denotes the power of external forces (volume and contact forces).

The first law of thermodynamics is the requirement that the change in energy (kinetic and internal) of a thermodynamic system balances the supply of energy through external forces and heat, mathematically expressed on the spatial configuration as

$$\begin{aligned} &\overline{\int_{\boldsymbol{\varphi}(\mathcal{B})} \rho e\,\mathrm{dV}}^{\boldsymbol{\cdot}} + \overline{\int_{\boldsymbol{\varphi}(\mathcal{B})} \frac{1}{2}\rho|\boldsymbol{v}|^2\,\mathrm{dV}}^{\boldsymbol{\cdot}} \\ &\quad = \int_{\boldsymbol{\varphi}(\mathcal{B})} \rho r\,\mathrm{dV} - \int_{\boldsymbol{\varphi}(\partial\mathcal{B})} \boldsymbol{q}\cdot\boldsymbol{n}\,\mathrm{dS} + \mathcal{P}_{ext}, \end{aligned} \tag{19}$$

where $\overline{(\,)}^{\boldsymbol{\cdot}}$ denotes the time derivative of a general integral, e and r are, respectively, the internal energy and the heat production per unit mass, and $\boldsymbol{q}$ is the heat flux per unit area.

The second law of thermodynamics postulates that the change in entropy is never less than the supply of entropy through heat, on the spatial configuration mathematically expressed as

$$\overline{\int_{\boldsymbol{\varphi}(\mathcal{B})} \rho\eta\,\mathrm{dV}}^{\boldsymbol{\cdot}} \geq \int_{\boldsymbol{\varphi}(\mathcal{B})} \frac{1}{\theta}\rho r\,\mathrm{dV} - \int_{\boldsymbol{\varphi}(\partial\mathcal{B})} \frac{1}{\theta}\boldsymbol{q}\cdot\boldsymbol{n}\,\mathrm{dS}. \tag{20}$$

By combination of Eqs. (18), (19) and (20), these global forms yield the fundamental inequality for every spatial point in $\boldsymbol{\varphi}(\mathcal{B})$

$$\boldsymbol{\sigma} : \boldsymbol{L} - \rho(\dot{e} - \theta\dot{\eta}) - \frac{1}{\theta}\boldsymbol{q}\cdot\nabla_s\theta \geq 0, \tag{21}$$

which, with the introduction of the Helmholtz free energy per unit mass, defined by $\psi \overset{\text{def}}{=} e - \theta\eta$, and Eq. (7), results in the following Clausius–Duhem inequality in terms of dissipation per unit reference volume as

$$\begin{aligned} &p\dot{\delta} + \boldsymbol{s} : \left(\bar{\boldsymbol{L}}^{\mathrm{e}} + \bar{\boldsymbol{V}}^{\mathrm{e}}\boldsymbol{L}^{\mathrm{t}}\bar{\boldsymbol{V}}^{e^{-1}} + \bar{\boldsymbol{V}}\boldsymbol{\Omega}\bar{\boldsymbol{V}}^{-1}\right) - \bar{\rho}(\dot{\psi} + \eta\dot{\theta}) \\ &\quad - \frac{J}{\theta}\boldsymbol{q}\cdot\nabla_s\theta \geq 0, \end{aligned} \tag{22}$$

where p and $\boldsymbol{s}$ are the spherical and deviatoric components of the Kirchhoff stress tensor, i.e., $\boldsymbol{\tau} = J\boldsymbol{\sigma} = p\mathbf{1} + \boldsymbol{s}$, and the reference mass density $\bar{\rho} = J\rho$ denotes the mass per unit reference volume.

Now, by substituting Eq. (9) into Eq. (22), one obtains the dissipation inequality

$$
\begin{aligned}
&(p-\partial_\delta\psi)\cdot\dot{\delta}+\left(\boldsymbol{s}-\partial_{\bar{\boldsymbol{h}}^{\mathrm{e}}}\psi\right):\bar{\boldsymbol{D}}^{\mathrm{e}}\\
&\quad+\left(\bar{\boldsymbol{V}}^{\mathrm{e}}\boldsymbol{s}\bar{\boldsymbol{V}}^{e^{-1}}-\partial_{\boldsymbol{h}^{\mathrm{t}}}\psi\right):\boldsymbol{D}^{\mathrm{t}}-(\eta+\partial_\theta\psi)\cdot\dot{\theta}\\
&\quad+\bar{\boldsymbol{V}}\boldsymbol{s}\bar{\boldsymbol{V}}^{-1}:\boldsymbol{\Omega}-\partial_\phi\psi\cdot\dot{\phi}-\partial_{\phi_s^f}\psi\cdot\dot{\phi}_s^f\\
&\quad-\partial_{\phi_s^r}\psi\cdot\dot{\phi}_s^r-\frac{J}{\theta}\boldsymbol{q}\cdot\nabla_s\theta\geq 0,
\end{aligned}
\tag{23}
$$

where $\partial_*\psi$ denotes the partial differential with respect to the state variables of the free energy function ψ. The principle of thermodynamic determinism requires that the above inequality holds for arbitrary thermodynamic process. Thus, for reversible process, any choice of $\{\dot{\delta}, \bar{\boldsymbol{D}}^{\mathrm{e}}, \dot{\theta}\}$ implies the constitutive equations

$$
p=\partial_\delta\psi,\quad \boldsymbol{s}=\partial_{\bar{\boldsymbol{h}}^{\mathrm{e}}}\psi \quad\text{and}\quad \eta=-\partial_\theta\psi,
\tag{24}
$$

and, for irreversible process, the following inequalities guarantee the nonnegative intrinsic dissipation in arbitrary evolution of $\{\boldsymbol{D}^{\mathrm{t}}, \boldsymbol{\Omega}, \dot{\phi}, \dot{\phi}_s^f, \dot{\phi}_s^r\}$

$$
\boldsymbol{A}^{\mathrm{t}}:\boldsymbol{D}^{\mathrm{t}}+\boldsymbol{A}^{\omega}:\boldsymbol{\Omega}+A^{\phi}\cdot\dot{\phi}+A^{f}\cdot\dot{\phi}_s^f+A^{r}\cdot\dot{\phi}_s^r\geq 0,
\tag{25}
$$

where $\{\boldsymbol{A}^{\mathrm{t}}, \boldsymbol{A}^{\omega}, A^{\phi}, A^{f}, A^{r}\}$ are the conjugate thermodynamic forces, defined as

$$
\begin{aligned}
&\boldsymbol{A}^{\mathrm{t}}=\bar{\boldsymbol{V}}^{\mathrm{e}}\boldsymbol{s}\bar{\boldsymbol{V}}^{e^{-1}}-\partial_{\boldsymbol{h}^{\mathrm{t}}}\psi,\quad \boldsymbol{A}^{\omega}=\bar{\boldsymbol{V}}\boldsymbol{s}\bar{\boldsymbol{V}}^{-1},\\
&A^{\phi}=-\partial_\phi\psi,\quad A^{f}=-\partial_{\phi_s^f}\psi,\quad A^{r}=-\partial_{\phi_s^r}\psi,
\end{aligned}
\tag{26}
$$

finally, for heat conduction process, the Fourier's law, $\boldsymbol{q}=-k\nabla_s\theta$, is taken to govern the heat flux and we obtain

$$
\frac{kJ}{\theta}|\nabla_s\theta|^2\geq 0,
\tag{27}
$$

where k is the nonnegative thermal conductivity, giving rise to an unconditional sanctification of the above inequality.

Further, by substituting the constitutive equations for the reversible processes, as shown in Eq. (24), into the Helmholtz free energy function, we obtain the following Gibbs relation in terms of the internal energy and entropy [50]:

$$
\begin{aligned}
\dot{e}-\theta\dot{\eta}&=p\cdot\dot{\delta}+\boldsymbol{s}:\bar{\boldsymbol{D}}^{\mathrm{e}}+\partial_{\boldsymbol{h}^{\mathrm{t}}}\psi:\boldsymbol{D}^{\mathrm{t}}+\partial_\phi\psi\cdot\dot{\phi}\\
&\quad+\partial_{\phi_s^f}\psi\cdot\dot{\phi}_s^f+\partial_{\phi_s^r}\psi\cdot\dot{\phi}_s^r.
\end{aligned}
\tag{28}
$$

Using the above equation, along with the definitions in Eq. (26), the conservation of energy can be written as the following entropy balance

$$
\theta\dot{\eta}=\boldsymbol{A}^{\mathrm{t}}:\boldsymbol{D}^{\mathrm{t}}+\boldsymbol{A}^{\omega}:\boldsymbol{\Omega}+A^{\phi}\cdot\dot{\phi}+A^{f}\cdot\dot{\phi}_s^f+A^{r}\cdot\dot{\phi}_s^r+r-\nabla_s\cdot\boldsymbol{q}.
\tag{29}
$$

For the sake of thermodynamic consistency, we postulate that the entropy potential depends on the same state variables as the Helmholtz free energy ψ , i.e., $\eta=\eta(\delta, \bar{\boldsymbol{h}}^{\mathrm{e}}, \boldsymbol{h}^{\mathrm{t}}, \theta, \phi, \phi_s^f, \phi_s^r)$, and obtain its time derivative

$$
\begin{aligned}
\dot{\eta}&=\partial_\delta\eta\cdot\dot{\delta}+\partial_{\bar{\boldsymbol{h}}^{\mathrm{e}}}\eta:\bar{\boldsymbol{D}}^{\mathrm{e}}+\partial_{\boldsymbol{h}^{\mathrm{t}}}\eta:\boldsymbol{D}^{\mathrm{t}}+\partial_\phi\eta\cdot\dot{\phi}\\
&\quad+\partial_{\phi_s^f}\eta\cdot\dot{\phi}_s^f+\partial_{\phi_s^r}\eta\cdot\dot{\phi}_s^r+\partial_\theta\eta\cdot\dot{\theta},
\end{aligned}
\tag{30}
$$

which, along with the introduction of the specific heat capacity $c=\theta\partial_\theta\eta$ and Eq. (29), gives the following partial differential equation for the temperature:

$$
\begin{aligned}
c\dot{\theta}&=\boldsymbol{A}^{\mathrm{t}}:\boldsymbol{D}^{\mathrm{t}}+\boldsymbol{A}^{\omega}:\boldsymbol{\Omega}+A^{\phi}\cdot\dot{\phi}+A^{f}\cdot\dot{\phi}_s^f\\
&\quad+A^{r}\cdot\dot{\phi}_s^r+r-\nabla_s\cdot\boldsymbol{q}\\
&\quad-\theta\Big(\partial_\delta\eta\cdot\dot{\delta}+\partial_{\bar{\boldsymbol{h}}^{\mathrm{e}}}\eta:\bar{\boldsymbol{D}}^{\mathrm{e}}+\partial_{\boldsymbol{h}^{\mathrm{t}}}\eta:\boldsymbol{D}^{\mathrm{t}}+\partial_\phi\eta\cdot\dot{\phi}\\
&\quad+\partial_{\phi_s^f}\eta\cdot\dot{\phi}_s^f+\partial_{\phi_s^r}\eta\cdot\dot{\phi}_s^r\Big).
\end{aligned}
\tag{31}
$$

Equation (31) describes the temperature change in SMA due to the evolutions of the state variables and the heat supplies.

5 Constitutive equations

By substituting the Helmholtz free energy (9) into Eq. (24), we derive the spherical and deviatoric parts of the stress tensor, p and $\boldsymbol{s}$, as well as the entropy η:

$$
\begin{cases}
p=K\left[\delta-3\alpha(\theta-\theta_0)\right],\\
\boldsymbol{s}=\sum_{i=1}^{3}s_i\,\boldsymbol{e}_i^{\mathrm{e}}\otimes\boldsymbol{e}_i^{\mathrm{e}}\quad\text{where}\quad s_i=2\mu\bar{h}_i^{\mathrm{e}},\\
\eta=3\alpha K\delta+c\,(\ln\theta-\ln\theta_0)-\phi\Delta_\eta+\eta_0.
\end{cases}
\tag{32}
$$

In analogy, the substitution of the Helmholtz free energy (9) into Eq. (26) gives the explicit expressions of the thermodynamic forces

$$\begin{cases} \boldsymbol{A}^{\mathrm{t}} = \bar{\boldsymbol{V}}^{\mathrm{e}} \boldsymbol{s} \bar{\boldsymbol{V}}^{e^{-1}} - \mu^{\mathrm{t}} \boldsymbol{h}^{\mathrm{t}} - \iota^{\mathrm{t}} \boldsymbol{n}^{\mathrm{t}}, \\ A^{\phi} = -\Delta_{\eta}(\theta - \theta_0) - z^{\mathrm{t}}(\phi) - \iota^{\phi}, \\ A^{*} = -\iota^{*} \quad \text{where} \quad * \in \{f, r\}, \end{cases} \tag{33}$$

where $\boldsymbol{n}^{\mathrm{t}} = \frac{\boldsymbol{h}^{\mathrm{t}}}{\|\boldsymbol{h}^{\mathrm{t}}\|}$ denotes the direction of the transformation strain, and $z^{\mathrm{t}} = \partial_{\phi} g^{\mathrm{t}}$ is the phase transformation hardening function, given as

$$z^{\mathrm{t}} = \kappa \tan^{m}\left[\frac{1}{2}(a\phi + b)\pi\right] + w, \tag{34}$$

where the hardening parameters $\{\kappa, m, a, b, w\}$ control the smoothness at initiation and completion of phase transformation, and they obey the constraints: $\kappa > 0, 0 < m < 1, a > 0, b > 0, a + b < 1$. For details, please refer to the authors' previous paper [47].

The Lagrangian multipliers $\{\iota^{\mathrm{t}}, \iota^{\phi}, \iota^{*}\}$ in Eq. (33) are defined as:

$$\iota^{\mathrm{t}} = \partial \mathcal{I}_{[0,\mathcal{H}]}(\boldsymbol{h}^{\mathrm{t}}) = \begin{cases} \iota^{t-} \leq 0 & \text{if} \quad \|\boldsymbol{h}^{\mathrm{t}}\| = 0 \\ 0 & \text{if} \quad 0 < \|\boldsymbol{h}^{\mathrm{t}}\| < \mathcal{H} \\ \iota^{t+} \geq 0 & \text{if} \quad \|\boldsymbol{h}^{\mathrm{t}}\| = \mathcal{H}, \end{cases} \tag{35}$$

$$\iota^{\phi} = \partial \mathcal{I}_{[0,1]}(\phi) = \begin{cases} \iota^{\phi-} \leq 0 & \text{if} \quad \phi = 0 \\ 0 & \text{if} \quad 0 < \phi < 1 \\ \iota^{\phi+} \geq 0 & \text{if} \quad \phi = 1, \end{cases} \tag{36}$$

$$\iota^{*} = \partial \mathcal{I}_{(0,1)}(\phi_s^f, \phi_s^r) = \begin{cases} \iota^{*-} \leq 0 & \text{if} \quad \phi_s^* - 0(\phi_s^*) = 0 \\ 0 & \text{if} \quad 0 < \phi_s^* < 1 \\ \iota^{*+} \geq 0 & \text{if} \quad \phi_s^* + 0(\phi_s^*) = 1, \end{cases} \tag{37}$$

where $0(\phi_s^*)$ is an same-order infinitesimal of ϕ_s^*, and the above three Lagrangian multipliers and their corresponding physical constraints obey the classical Kuhn–Tucker conditions.

According to the literature of [51] and [52], the principle of maximum dissipation implies the transformation strain is solely linked to the martensite volume fraction when martensite reorientation is suppressed. Thus, we assume the following evolution equation:

$$\boldsymbol{D}^{\mathrm{t}} = \dot{\phi} \mathcal{H} \boldsymbol{\Lambda}, \quad \boldsymbol{\Lambda} = \begin{cases} \frac{\boldsymbol{s}}{\|\boldsymbol{s}\|} & \text{if} \quad \dot{\phi} \geq 0 \\ \boldsymbol{n}^{\mathrm{t}} & \text{if} \quad \dot{\phi} < 0 \end{cases} \tag{38}$$

which means during forward transformation, the transformation strain grows by the direction of the deviatoric stress tensor, while during reverse transformation, the transformation strain recovers in its own direction.

With regard to the internal variables ϕ_s^f and ϕ_s^r, we introduce the following indicator function to control them

$$\dot{\phi_s^f} = \mathcal{I}^f \dot{\phi}, \quad \mathcal{I}^f = \begin{cases} 0 & \text{if} \quad \dot{\phi} \geq 0 \\ 1 & \text{if} \quad \dot{\phi} < 0 \end{cases} \tag{39}$$

$$\dot{\phi_s^r} = \mathcal{I}^r \dot{\phi}, \quad \mathcal{I}^r = \begin{cases} 1 & \text{if} \quad \dot{\phi} > 0 \\ 0 & \text{if} \quad \dot{\phi} \leq 0 \end{cases} \tag{40}$$

The above two evolution laws imply that ϕ_s^f decreases during the reverse phase transformation, while ϕ_s^r increases during the forward phase transformation, which get initialized at each turning point of the phase transformation

$$\begin{cases} \phi_s^f = \phi_s^r & \text{if} \quad \ddot{\phi} < 0 \\ \phi_s^r = \phi_s^f & \text{if} \quad \ddot{\phi} > 0 \end{cases} \tag{41}$$

According to the above rules, ϕ_s^f jumps to ϕ_s^r when the phase transformation turns from "Forward" to "Reverse" (the second-order derivative of the martensite volume fraction $\ddot{\phi}$ is less than zero), while ϕ_s^r jumps to ϕ_s^f in the opposite case (R → F).

Now, with all internal variables linked to the changes of martensite volume fraction ϕ as formulated above, the inequality (25) reads

$$\underbrace{\left(\mathcal{H}\boldsymbol{A}^{\mathrm{t}} : \boldsymbol{\Lambda} + A^{\phi} + A^{f}\mathcal{I}^{f} + A^{r}\mathcal{I}^{r}\right)}_{\Gamma} \cdot \dot{\phi} \geq 0, \tag{42}$$

which is guaranteed by the following choice of the evolution equation associated with the phase transformation

$$\dot{\phi} = \dot{\gamma} \mathcal{S}(\Gamma), \tag{43}$$

where $\dot{\gamma}$ is a nonnegative multiplier, and $\mathcal{S}(\cdot)$ is a sign function to extract the sign of the total thermodynamic force Γ.

By substituting Eqs. $(32)_3$ and (42) into Eq. (31), we obtain the temperature evolution equation as

$$c\dot{\theta} = \left(\Gamma + \Delta_{\eta}\theta\right) \cdot \dot{\phi} - 3\alpha K \theta \dot{\delta} + r - \nabla_s \cdot \boldsymbol{q}. \tag{44}$$

To determine the boundary between the elasticity and phase transformation, we define a yield criterion, in terms of the thermodynamic force, for the initiation, growth and saturation of the phase transformation

$$\Phi = |\mathit{\Gamma}| - Y(\phi, \phi_s^f, \phi_s^r), \tag{45}$$

where $Y(\phi, \phi_s^f, \phi_s^r)$ is the threshold for the phase transformation, depending on the martensite volume fraction ϕ as follows:

- if the material is located on the main hysteresis loop, the parameter Y takes the reference value

$$Y = Y_0 \tag{46}$$

- if the material is located on the forward internal hysteresis loop, the parameter Y takes

$$Y(\phi) = \left[1 - \phi_s^f\left(\frac{1-\phi}{1-\phi_s^f}\right)\right] Y_0, \quad 0 < \phi_s^f < 1 \tag{47}$$

- if the material is located on the reverse internal hysteresis loop, the parameter Y takes

$$Y(\phi) = \left(1 + \phi - \frac{\phi}{\phi_s^r}\right) Y_0, \quad 0 < \phi_s^r < 1 \tag{48}$$

where Y_0 is the model parameter. The above logic expression describes the change of internal hysteresis loop when SMA is subjected to incomplete phase transformation. The evolution Eq. (43) and the yield function (45) are complemented by the following loading–unloading conditions

$$\dot{\gamma} \geq 0, \qquad \Phi \leq 0, \qquad \dot{\gamma}\Phi = 0. \tag{49}$$

In summary, the overall phase transformation laws are as follows:

- If the yield function $\Phi < 0$, and martensite phase transformation does not occur, then the internal variables $\dot{\phi} = 0, \quad \boldsymbol{D}^{\mathrm{t}} = \boldsymbol{0}, \quad \dot{\phi}_s^r = 0, \quad \dot{\phi}_s^r = 0.$
- If the yield function $\Phi = 0$, the thermodynamic driving force $\mathit{\Gamma} > 0$ and the martensite volume fraction $\phi < 1$, and the forward martensite phase transformation occurs (A→M), then the internal variables evolve as $\dot{\phi} = \dot{\gamma}, \quad \boldsymbol{D}^{\mathrm{t}} = \mathcal{H}\dot{\phi}\frac{\boldsymbol{s}}{\|\boldsymbol{s}\|}, \quad \dot{\phi}_s^r = 0, \quad \dot{\phi}_s^r = \dot{\phi}.$
- If the yield function $\Phi = 0$, the thermodynamic driving force $\mathit{\Gamma} < 0$ and the martensite volume fraction $\phi > 0$, and the reverse martensite phase transformation occurs (M→A), then the internal variables evolve as $\dot{\phi} = -\dot{\gamma}, \quad \boldsymbol{D}^{\mathrm{t}} = \mathcal{H}\dot{\phi}\boldsymbol{n}^{\mathrm{t}}, \quad \dot{\phi}_s^r = \dot{\phi}, \quad \dot{\phi}_s^r = 0.$

Here, it is noted that once the internal variables, $\boldsymbol{h}^{\mathrm{t}}$, ϕ, ϕ_s^f and ϕ_s^r, arrive their boundaries, the Kuhn–Tucker complementary conditions will be activated to compute the Lagrangian multipliers, ι^t, ι^{ϕ}, ι^f and ι^r. For example, when the transformation strain $\boldsymbol{h}^{\mathrm{t}}$ arrives the boundary $\mathcal{H}$, the complementary condition $\{\iota^t \geq 0, \|\boldsymbol{h}^{\mathrm{t}}\| - \mathcal{H} \leq 0, \iota^t(\|\boldsymbol{h}^{\mathrm{t}}\| - \mathcal{H}) = 0\}$ is solved to obtain ι^t. Through Eqs. (38)–(40), evolutions of the internal variables, $\boldsymbol{h}^{\mathrm{t}}$, ϕ_s^f and ϕ_s^r, have been linked to phase transformation process. Thus, the issue comes down to the solution of the transformation multiplier $\dot{\gamma}$, which will be addressed in the following section, and the iterative formula is given in Eq. (59).

6 Numerical implementation

In this section, we present a numerical integration algorithm for the proposed constitutive equations so that the model can be used as computational tool for the analysis of SMA boundary value problems. First, we adopt a backward Euler scheme to discretize the constitutive equations to obtain the corresponding incremental forms within a pseudotime interval. Then, we solve the return-mapping scheme using the cutting-plane algorithm, which is an iterative procedure for numerical solution of the return-mapping problem.

6.1 Euler discretization: the incremental elastic-transformation constitutive problem

The deformation-driven initial value problem of the proposed constitutive model is described as: Given the deformation gradient $\boldsymbol{F}_n$, the internal state variables $\boldsymbol{h}_n^{\mathrm{t}}, \phi_n, {\phi_s^f}_n, {\phi_s^r}_n$, and the temperature θ_n at the beginning of the pseudotime interval $[t_n, t_{n+1}]$, and given the incremental deformation gradient $\boldsymbol{F}_{\triangle}$ for this interval, find the solutions for the state variables and temperature at the end of this interval satisfying the discretized constitutive equations.

The numerical discretization of the evolution Eq. (38), by means of the backward exponential integration scheme, leads to the update formula for the transformation deformation gradient

$$\boldsymbol{V}^{\mathrm{t}}_{n+1} = \exp\left[\Delta\gamma\mathcal{S}(\mathit{\Gamma}_{n+1})\mathcal{H}\boldsymbol{\Lambda}_{n+1}\right]\boldsymbol{V}^{\mathrm{t}}_{n}. \tag{50}$$

The temperature evolution Eq. (44) is discretized using the conventional backward Euler scheme, given as

$$\theta_{n+1} = \frac{c\theta_n + \mathit{\Gamma}_{n+1}\Delta\gamma\mathcal{S}(\mathit{\Gamma}_{n+1}) + r_{n+1} - \nabla_s\cdot\boldsymbol{q}_{n+1}}{c - \Delta_\eta\Delta\gamma\mathcal{S}(\mathit{\Gamma}_{n+1}) + 3\alpha K\Delta\delta}. \tag{51}$$

The initial value problem of the constitutive model is complemented by the time-discrete yield function (45) and loading–unloading conditions (49):

$$\begin{cases} \Phi_{n+1} = |\mathit{\Gamma}_{n+1}| - Y(\phi_{n+1}), \\ \Delta\gamma \geq 0, \quad \Phi_{n+1} \leq 0, \quad \Delta\gamma\Phi_{n+1} = 0. \end{cases} \tag{52}$$

To solve the above initial value problem, we adopt a two-step elastic predictor/transformation corrector algorithm, as follows:

- The elastic trial step.
  Firstly, we assume that the transformation multiplier $\Delta\gamma = 0$, that is, the step over the time interval $[t_n, t_{n+1}]$ is purely elastic. The elastic trial solution is obtained by setting all dissipative internal variables unchanged. The introduction of the multiplicative decomposition $\bar{\boldsymbol{V}} = \bar{\boldsymbol{V}}^{\mathrm{e}}\boldsymbol{V}^{\mathrm{t}}$ into Eq. (50) results in the elastic trial state

  $$\bar{\boldsymbol{V}}^{\mathrm{e}}_{n+1} = \bar{\boldsymbol{V}}^{e\ \mathrm{trial}}_{n+1}\exp\left[-\Delta\gamma\mathcal{S}(\mathit{\Gamma}_{n+1})\mathcal{H}\boldsymbol{\Lambda}_{n+1}\right], \tag{53}$$

  where $\bar{\boldsymbol{V}}^{e\ \mathrm{trial}}_{n+1} = \bar{\boldsymbol{V}}_{\triangle}\bar{\boldsymbol{V}}^{\mathrm{e}}_{n}$ is the trial elastic stretch tensor, and $\bar{\boldsymbol{V}}_{\triangle}$ is the incremental stretch tensor. In the absence of martensite reorientation, we further assume that elastic and transformation are isotropy, that is, $\bar{\boldsymbol{V}}^{\mathrm{e}}$ and $\boldsymbol{\Lambda}$ commute. For a more rigorous discussion of this claim and the following derivation, the reader is referred to Sect. 3.2 A Hencky strain return-mapping algorithm in the work of [47]. Then, by taking the tensor logarithm of Eq. (53), we obtain an infinitesimal formula in terms of the Eulerian Hencky strain tensors

  $$\bar{\boldsymbol{h}}^{\mathrm{e}}_{n+1} = \bar{\boldsymbol{h}}^{e\ \mathrm{trial}}_{n+1} - \Delta\gamma\mathcal{S}(\mathit{\Gamma}_{n+1})\mathcal{H}\boldsymbol{\Lambda}_{n+1}, \tag{54}$$

  where $\bar{\boldsymbol{h}}^{e\ \mathrm{trial}}_{n+1} = \ln\bar{\boldsymbol{V}}^{e\ \mathrm{trial}}_{n+1}$ denotes the trial elastic Hencky strain. The corresponding trial stress is given by

  $$\boldsymbol{s}^{\mathrm{trial}}_{n+1} = 2\mu\bar{\boldsymbol{h}}^{e\ \mathrm{trial}}_{n+1}. \tag{55}$$

  The trial stress in Eq. (55) is called admissible stress if the yield function $(52)_1$ in the trial state satisfies $\Phi^{\mathrm{trial}}_{n+1} \leq 0$. Namely, the elastic trial state lies inside of the yield surface and itself is the actual solution. In this case, we update all state quantities as $(\cdot)_{n+1} = (\cdot)^{\mathrm{trial}}_{n+1}$, and the algorithm is terminated. Otherwise, the elastic trial state is not admissible and the transformation corrector step presented below will be activated to find the solution to the initial value problem.
- The transformation corrector step.
  When the phase transformation process takes place within the time interval $[t_n, t_{n+1}]$, the transformation multiplier has to be strictly positive $\Delta\gamma > 0$. The transformation corrector step then consists in finding the actual solution of the following algebraic system written with the above elastic trial state definition:

  $$\begin{cases} \bar{\boldsymbol{h}}^{\mathrm{e}}_{n+1} - \bar{\boldsymbol{h}}^{e\ \mathrm{trial}}_{n+1} + \Delta\gamma\mathcal{S}(\mathit{\Gamma}_{n+1})\mathcal{H}\boldsymbol{\Lambda}_{n+1} = \boldsymbol{0}, \\ \theta_{n+1} - \frac{(c+3\alpha K\Delta\delta)\theta^{\mathrm{trial}}_{n} + \mathit{\Gamma}_{n+1}\Delta\gamma\mathcal{S}(\mathit{\Gamma}_{n+1}) + r_{n+1} - \nabla_s\cdot\boldsymbol{q}_{n+1}}{c - \Delta_\eta\Delta\gamma\mathcal{S}(\mathit{\Gamma}_{n+1}) + 3\alpha K\Delta\delta} = 0, \\ \phi_{n+1} - \phi^{\mathrm{trial}}_{n+1} - \Delta\gamma\mathcal{S}(\mathit{\Gamma}_{n+1}) = 0, \\ \phi^{f}_{s\ n+1} - \phi^{f\ \mathrm{trial}}_{s\ n+1} - \mathcal{I}^{f}_{n+1}\Delta\gamma\mathcal{S}(\mathit{\Gamma}_{n+1}) = 0, \\ \phi^{r}_{s\ n+1} - \phi^{r\ \mathrm{trial}}_{s\ n+1} - \mathcal{I}^{r}_{n+1}\Delta\gamma\mathcal{S}(\mathit{\Gamma}_{n+1}) = 0, \\ \Phi_{n+1} = |\mathit{\Gamma}_{n+1}| - Y(\phi_{n+1}) = 0. \end{cases} \tag{56}$$

  The nonlinear Eq. (56) are solved using the cutting-plane return-mapping algorithm presented below.

6.2 Solution of the return-mapping equations: the cutting-plane algorithm

The cutting-plane algorithm is an iterative procedure for numerical solution of the return-mapping equations. In the cutting-plane iteration k, the yield function Φ_{n+1} is linearized about the current state quantities

$$
\begin{aligned}
&\Phi\left[\bar{\boldsymbol{h}}^{e\,(k)}_{n+1}, \theta^{(k)}_{n+1}, \phi^{(k)}_{n+1}, \phi^{f\,(k)}_{s\;n+1}, \phi^{r\,(k)}_{s\;n+1}\right]\\
&\quad + \partial_{\bar{\boldsymbol{h}}^{e\,(k)}_{n+1}}\Phi : \left[\bar{\boldsymbol{h}}^{e\,(k+1)}_{n+1} - \bar{\boldsymbol{h}}^{e\,(k)}_{n+1}\right]\\
&\quad + \partial_{\theta^{(k)}_{n+1}}\Phi \cdot \left[\theta^{(k+1)}_{n+1} - \theta^{(k)}_{n+1}\right]\\
&\quad + \partial_{\phi^{(k)}_{n+1}}\Phi \cdot \left[\phi^{(k+1)}_{n+1} - \phi^{(k)}_{n+1}\right]\\
&\quad + \partial_{\phi^{f\,(k)}_{s\;n+1}}\Phi \cdot \left[\phi^{f\,(k+1)}_{s\;n+1} - \phi^{f\,(k)}_{s\;n+1}\right]\\
&\quad + \partial_{\phi^{r\,(k)}_{s\;n+1}}\Phi \cdot \left[\phi^{r\,(k+1)}_{s\;n+1} - \phi^{r\,(k)}_{s\;n+1}\right] = 0, \qquad (57)
\end{aligned}
$$

where $\{\bar{\boldsymbol{h}}^{e\,(k+1)}_{n+1}, \theta^{(k+1)}_{n+1}, \phi^{(k+1)}_{n+1}, \phi^{f\,(k+1)}_{s\;n+1}, \phi^{r\,(k+1)}_{s\;n+1}\}$ are the state quantities in a new iteration $k+1$. To solve Eq. (57), we apply the forward Euler scheme on the constitutive Eqs. $(56)_{1-5}$ and obtain the formula

$$
\begin{cases}
\bar{\boldsymbol{h}}^{e\,(k+1)}_{n+1} - \bar{\boldsymbol{h}}^{e\,(k)}_{n+1} = \Delta\gamma\left[-\mathcal{S}(\Gamma^{(k)}_{n+1})\mathcal{H}\boldsymbol{\Lambda}^{(k)}_{n+1}\right],\\
\theta^{(k+1)}_{n+1} - \theta^{(k)}_{n+1} = \Delta\gamma\left[\frac{\Delta_\eta \mathcal{S}(\Gamma^{(k)}_{n+1})\theta^{(k)}_{n+1} + \Gamma^{(k)}_{n+1}\mathcal{S}(\Gamma^{(k)}_{n+1})}{c - \Delta_\eta \Delta\gamma \mathcal{S}(\Gamma_{n+1}) + 3\alpha K \Delta\delta}\right],\\
\phi^{(k+1)}_{n+1} - \phi^{(k)}_{n+1} = \Delta\gamma\left[\mathcal{S}(\Gamma^{(k)}_{n+1})\right],\\
\phi^{f\,(k+1)}_{s\;n+1} - \phi^{f\,(k)}_{s\;n+1} = \Delta\gamma\left[\mathcal{I}^{f\,(k)}_{n+1}\mathcal{S}(\Gamma^{f\,(k)}_{n+1})\right],\\
\phi^{r\,(k+1)}_{s\;n+1} - \phi^{r\,(k)}_{s\;n+1} = \Delta\gamma\left[\mathcal{I}^{r\,(k)}_{n+1}\mathcal{S}(\Gamma^{r\,(k)}_{n+1})\right].
\end{cases}
\qquad (58)
$$

With the substitution of Eq. (58) into (57), we obtain the following closed form of the transformation multiplier

$$
\Delta\gamma = \Phi^{(k)}/D^{(k)}_{n+1}, \qquad (59)
$$

where

$$
\begin{aligned}
D^{(k)}_{n+1} =& \partial_{\bar{\boldsymbol{h}}^{e\,(k)}_{n+1}}\Phi : \left[-\mathcal{S}(\Gamma^{(k)}_{n+1})\mathcal{H}\boldsymbol{\Lambda}^{(k)}_{n+1}\right]\\
&+ \partial_{\theta^{(k)}_{n+1}}\Phi \cdot \left[\frac{\Delta_\eta \mathcal{S}(\Gamma^{(k)}_{n+1})\theta^{(k)}_{n+1} + \Gamma^{(k)}_{n+1}\mathcal{S}(\Gamma^{(k)}_{n+1})}{c - \Delta_\eta \Delta\gamma \mathcal{S}(\Gamma_{n+1}) + 3\alpha K \Delta\delta}\right]\\
&+ \partial_{\phi^{(k)}_{n+1}}\Phi \cdot \left[\mathcal{S}(\Gamma^{(k)}_{n+1})\right]\\
&+ \partial_{\phi^{f\,(k)}_{s\;n+1}}\Phi \cdot \left[\mathcal{I}^{f\,(k)}_{n+1}\mathcal{S}(\Gamma^{f\,(k)}_{n+1})\right]\\
&+ \partial_{\phi^{r\,(k)}_{s\;n+1}}\Phi \cdot \left[\mathcal{I}^{r\,(k)}_{n+1}\mathcal{S}(\Gamma^{r\,(k)}_{n+1})\right]. \qquad (60)
\end{aligned}
$$

By substituting the obtained $\Delta\gamma$ into Eq. (58), we then compute all state quantities in iteration $k+1$. Starting from the initial condition, ($k=0$), of the cutting-plane algorithm

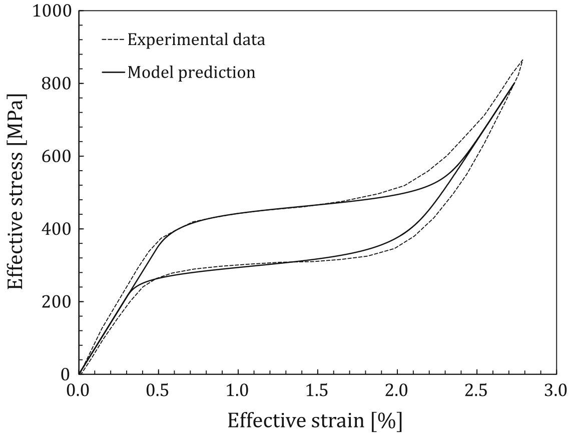

Fig. 2 The main hysteresis stress–strain loop in pseudoelastic NiTi wire: model prediction and experimental data reported by [29]; model parameters are calibrated using this input data

$$
\begin{aligned}
&\left\{\bar{\boldsymbol{h}}^{e\,(0)}_{n+1}, \theta^{(0)}_{n+1}, \phi^{(0)}_{n+1}, \phi^{f\,(0)}_{s\;n+1}, \phi^{r\,(0)}_{s\;n+1}\right\}\\
&\quad = \left\{\bar{\boldsymbol{h}}^{e\ \mathrm{trial}}_{n+1}, \theta^{\mathrm{trial}}_{n+1}, \phi^{\mathrm{trial}}_{n+1}, \phi^{f\ \mathrm{trial}}_{s\;n+1}, \phi^{r\ \mathrm{trial}}_{s\;n+1}\right\}, \qquad (61)
\end{aligned}
$$

we can produce a sequence of states by repeating the above iteration procedure

$$
\left\{\bar{\boldsymbol{h}}^{e\,(k)}_{n+1}, \theta^{(k)}_{n+1}, \phi^{(k)}_{n+1}, \phi^{f\,(k)}_{s\;n+1}, \phi^{r\,(k)}_{s\;n+1}\right\}, \qquad k = 0, 1, 2... \qquad (62)
$$

The cutting-plane iteration will be interrupted when the yield function satisfies the convergence criterion

$$
\Phi\left(\bar{\boldsymbol{h}}^{e\,(k)}_{n+1}, \theta^{(k)}_{n+1}, \phi^{(k)}_{n+1}, \phi^{f\,(k)}_{s\;n+1}, \phi^{r\,(k)}_{s\;n+1}\right) \le \epsilon_{tol}, \qquad (63)
$$

where ϵ_{tol} is the convergence tolerance. Inequality (63) indicates the yield function in state k is sufficiently close to zero, and the numerical solution at present state is in accordance with the transformation consistency.

7 Model validation

In order to use the model as a computational tool for the SMA boundary value problem, we implement the above numerical algorithm into the commercial FE software ABAQUS/Explicit by means of

Table 1 Model parameters

Parameters	Values/units	Parameters	Values/units
K	57,390 MPa	μ	26,488 MPa
α	22×10^{-6}/K	κ	2.2 MPa
a	0.996	b	0.002
m	0.16	ω	− 6.2 MPa
Y_0	1.22 MPa	Δ_η	0.3 MPa/K
$\mathcal{H}$	0.0154	θ_0	265 K

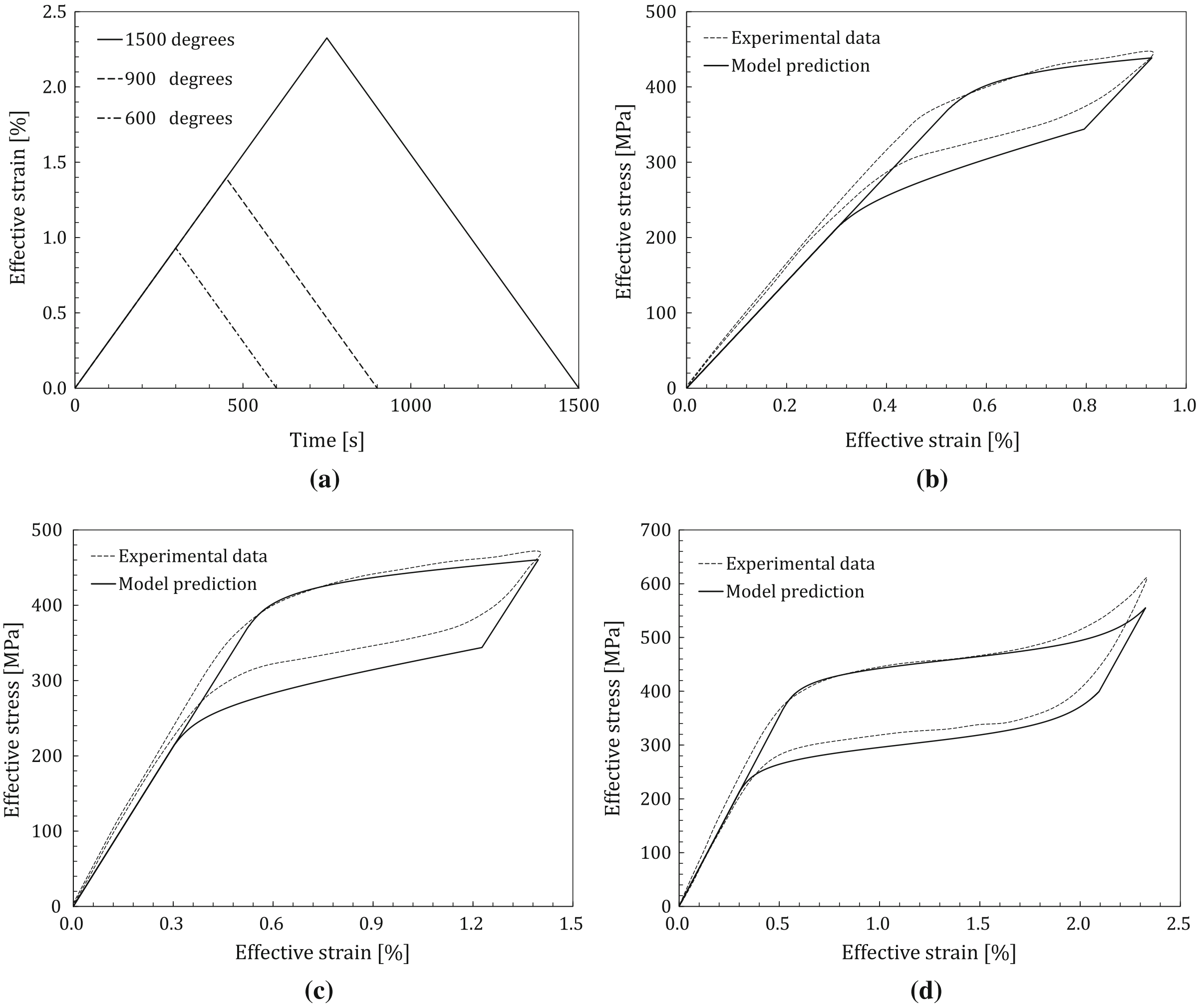

(a) (b)

(c) (d)

Fig. 3 The internal hysteresis stress–strain loops under partial load–unload conditions with three twist degrees of 600, 900 and 1500; the model predictions are compared to the experimental data [29]

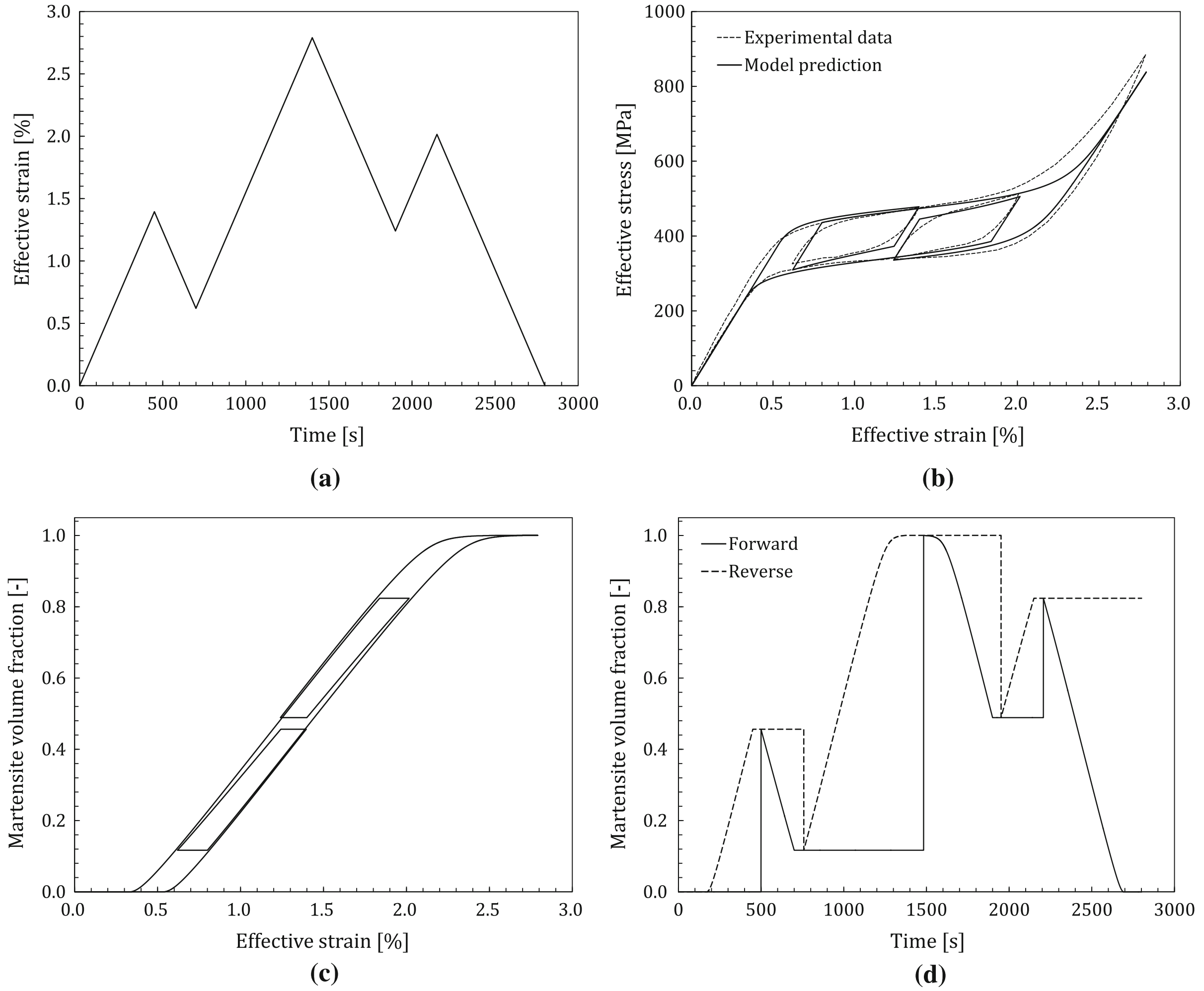

Fig. 4 The internal hysteresis loops during both loading and unloading cycles: **a** loading path, **b** comparison between model prediction and experimental data [29], **c** evolution of martensite volume fraction, **d** change of transition points for both forward and reverse phase transformations

a user-defined material subroutine VUMAT. Numerical efficiency and accuracy of the model are validated against the experimental data of [29] on NiTi SMA wires.

Figure 2 shows the main hysteresis stress–strain loop in pseudoelastic NiTi wire, and the model prediction is compared to the experimental data of [29]. Model parameters are calibrated by this experimental data and listed in Table 1, and they will be used in the following predictions with various internal hysteresis loops. It is noted that the experimental data are obtained from the twist test up to 1800 degrees on SMA wire, at such twist degree the wire undergoes a complete phase transformation process and displays the main hysteresis loop with the maximum effective strain of 2.8%. Overall, the model prediction agrees reasonably well with the experimental data by capturing the pseudoelastic hysteresis stress–strain loop, the complete shape recovery and the smooth transition at the initiation and completion of phase transformation.

Figure 3 shows the internal hysteresis stress–strain loops under partial load–unload conditions. Specifically, Fig. 3a gives the loading paths, and the twist degrees of 600, 900 and 1500 can generate the maximum strains of 0.93%, 1.40% and 2.32%, respec-

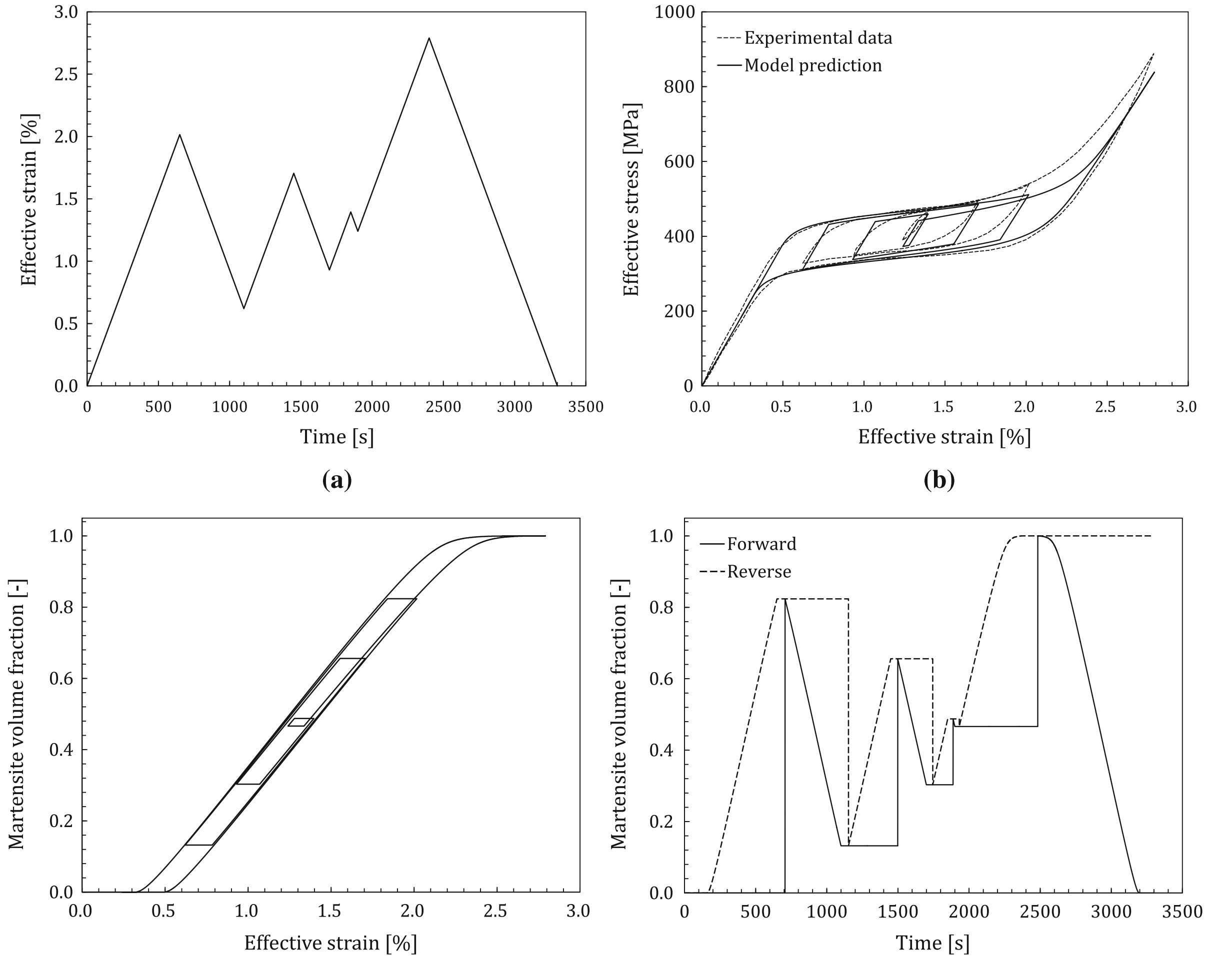

(a) (b) (c) (d)

Fig. 5 The complex internal hysteresis loops during loading cycle: **a** loading path, **b** comparison between model prediction and experimental data [29], **c** evolution of martensite volume fraction, **d** change of transition points for both forward and reverse phase transformations

tively. Figure 3b–d compares the model predictions to the experimental data. It can be seen from the figures that with the increase in the loading degree, both the height and width of the hysteresis loop increase as well; namely, the size of internal hysteresis loop highly depends on the loading degree. The model predictions reasonably describe the simple internal loops under the partial load–unload conditions. However, during the reverse phase transformation from martensite to austenite, the model predictions deviate from the experimental data, especially at lower loading degrees of 600 and 900. This is mainly because the model parameters are calibrated just using the main hysteresis loop data along with no internal loop information.

Figures 4, 5 and 6 show several examples of complex internal hysteresis loops during loading and unloading cycles. In Fig. 4, sub-figure (a) shows the loading path, and the effective strain varies as 0, 1.39%, 0.62%, 2.79%, 1.24%, 2.02%, 0 within the total loading time of 2800 s. Sub-figure (b) plots the internal hysteresis stress–strain loops during both forward and reverse phase transformations. Model prediction has a good agreement with the experimental data by capturing both main and internal hysteresis loops. The only deficiency is that the material response shows abrupt

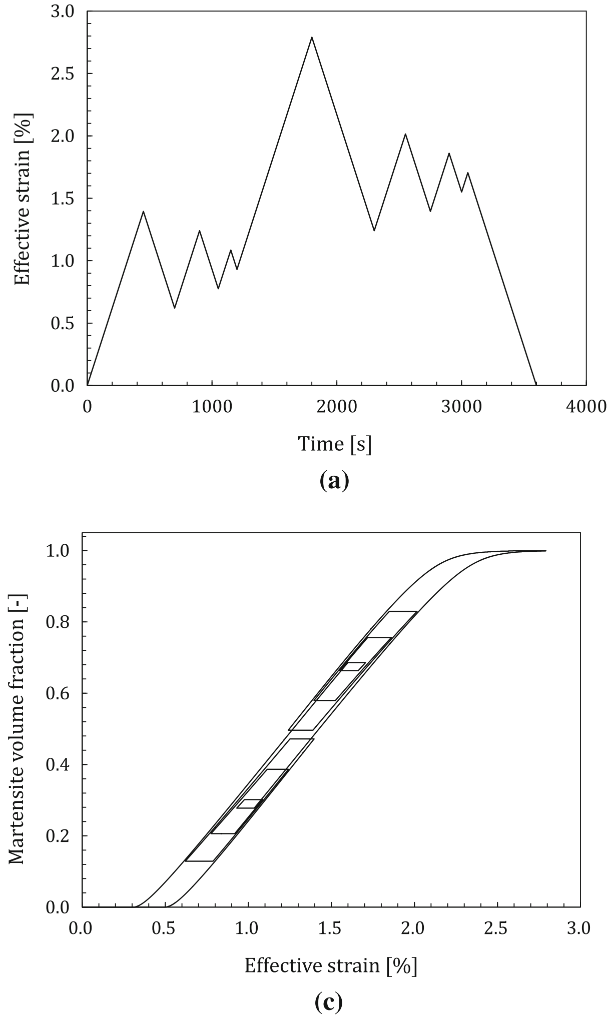

(a) (b) (c) (d)

Fig. 6 The complex internal hysteresis loops during both loading and unloading cycles: **a** loading path, **b** comparison between model prediction and experimental data [29], **c** evolution of martensite volume fraction, **d** change of transition points for both forward and reverse phase transformations

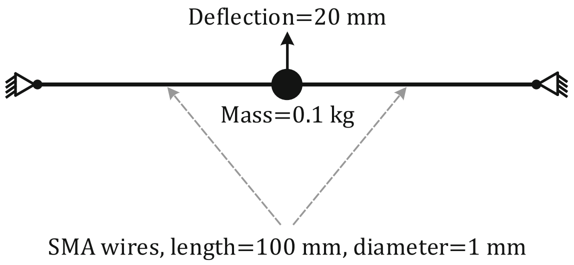

Fig. 7 Schematic representation of the vibration system, comprising a mass and two antagonistic SMA wires

transitions at the initiation and completion of the internal hysteresis loops. This phenomenon is due to an assumption in the proposed model that the incomplete phase transformation shares the same hardening function with the complete phase transformation, which can be addressed by the introduction of another smooth hardening function for the incomplete phase transformation process. Sub-figure (c) shows the evolution of martensite volume fraction ϕ during the phase transformation process. Likewise, the curve shows internal hysteresis loops, indicating that the internal hysteresis loops on the stress–strain curve can be physically attributed to the incomplete phase transformation during both forward and reverse phase transformation processes. Sub-figure (d) shows the evolution

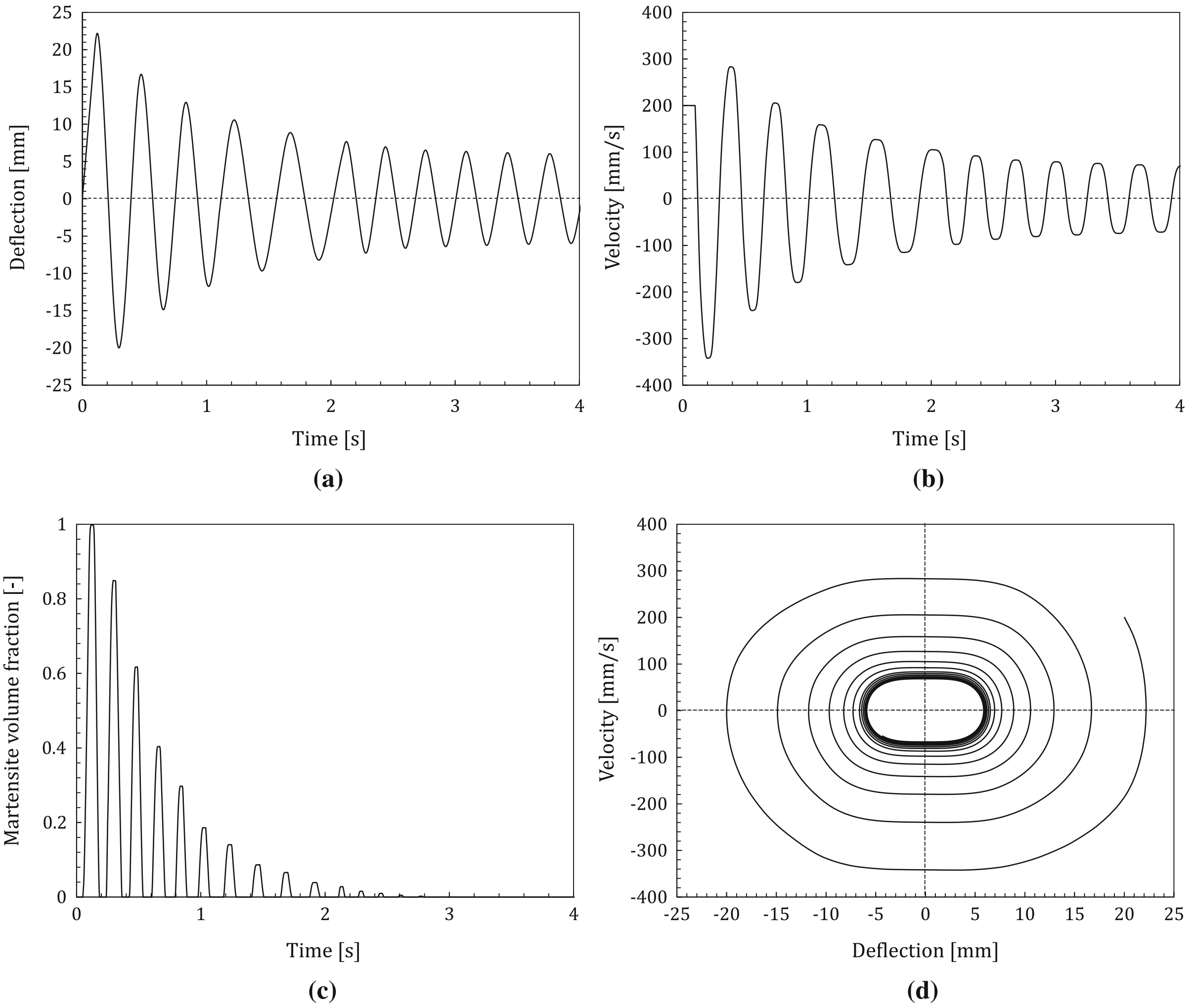

(a) (b) (c) (d)

Fig. 8 Free vibration behavior of the system: **a** deflection, **b** velocity, **c** martensite volume fraction, **d** velocity versus deflection

of the internal state variables ϕ_s^f and ϕ_s^r during the phase transformation process. These two variables represent the transition points of the internal hysteresis loop during the forward and reverse phase transformations. They evolve with the martensite volume fraction ϕ according to Eqs. (39) and (40). By combination of sub-figure (a), it is observed that at loading period, ϕ_s^r increases, while ϕ_s^f remains unchanged, vice versa. At each turning point, the unchanged one jumps to the value of another. For example, at the first turning point with strain of 1.39%, ϕ_s^f jumps to 0.46, that is, the value of ϕ_s^r. Figures 5 and 6 provide other two more complex examples of the internal hysteresis loops. Overall, the model shows good predictive capability and can be used for various complex loading conditions.

8 Dynamic analysis

Pseudoelastic SMA shows remarkable hysteresis effect as shown in the figures of Sect. 7, implying that a large amount of energy is dissipated during phase transformation process. This pseudoelastic hysteresis indicates high damping capacity and thereby can be used for energy absorption under dynamic loadings. To demonstrate the superiority of SMA in vibration control, we present a dynamic analysis of a vibration system comprising a mass and two antagonistic SMA wires, as shown in Fig. 7. The SMA wires have length of 100 mm and diameter of 1 mm, the two far ends are fixed on hinges, and the middle ends were linked to a mass of 0.1 kg. The mass is subjected to an initial deflection of 20 mm within the first 0.1 s to induce free vibration behavior of the system.

Figure 8 shows the free vibration behavior of the above system. The mass displays a sinusoidal oscillation with frequency of about 3 Hz, as shown in the first diagram. The second diagram shows the corresponding velocity of the mass, and the oscillation has a half-cycle hysteresis compared to the deflection. Upon the release of the applied load, the oscillation amplitude gradually decreases and finally tends to be constant. This vibration reduction phenomenon is mainly because the kinetic energy of the vibration system is continuously dissipated during the repeated phase transformation processes. In the third diagram, the evolution of martensite volume fraction on the SMA wire is plotted. The maximum value of 1 in the first cycle represents the complete phase transformation on the SMA wire. Afterward, phase transformation degrades with the number of vibration cycles and finally stops after 3 s. The last diagram combines the velocity and the deflection, allowing for an illustrative interpretation of the free vibration process. During the free vibration process, the kinetic and potential energies convert mutually and the total energy drops gradually. Eventually, when the decreasing energy is insufficient to initiate phase transformation on the SMA wires, the vibration system enters the elastic regime and reaches a dynamic steady state.

9 Numerical example

To demonstrate the capabilities of the model in solving SMA boundary value problem with incomplete phase transformation case, a crack SMA specimen under incomplete loading–unloading condition is simulated in this section. The finite element model of the crack SMA specimen is shown in Fig. 9, with the thickness of 1 mm. The height and width of the specimen are 20 mm, and the opening angle of the crack is 30 degree. In order to improve the numerical accuracy and capture the local response, the mesh around the crack tip is refined.

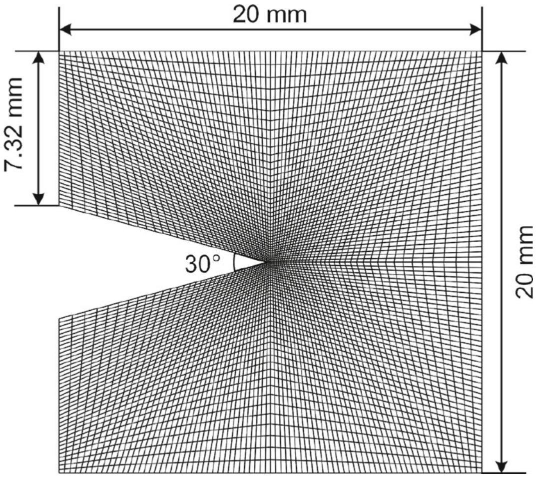

Fig. 9 Finite element model of the crack SMA specimen

During the simulation, the forces are applied on the top and bottom ends of the specimen. The loading path is sequentially 0, 1.25 kN, 0.75 kN, 1.75 kN, 1 kN, 1.5 kN, 0, as shown in Fig. 10a. It comprises four stages: partial loading (O→A), incomplete unloading–loading (A→B→C), partial unloading (C→D) and incomplete loading–unloading (D→E→O), which will generate both main and internal hysteresis loops. Figure 10b shows the global force–displacement response of the crack SMA specimen. At the first stage, the force–displacement curve shows nonlinearity indicating that phase transformation has occurred on the specimen. Then, at the second stage, an internal loop is observed during the forward phase transformation process. Subsequently, the partial unloading from the maximum loading point C to point D induces reverse phase transformation from martensite to austenite. Finally, the incomplete loading–unloading leads to an internal loop during the reverse phase transformation. Upon the complete unloading, the force–displacement curve returns to the original point O, showing a complete shape recovery. Overall, the simulation result well demonstrates the prime characteristics of SMA such as pseudoelasticity, main and internal hysteresis loops.

With regard to the local response around the crack tip on the SMA specimen, Figs. 11 and 12 display the martensite volume fraction and Mises stress contour plots, respectively. The evolution of the phase transformation zone and stress distribution on the SMA specimen are well demonstrated throughout the incomplete phase transformation process. At point A, with the increasing stress concentration, material around the crack tip transforms from austenite to martensite.

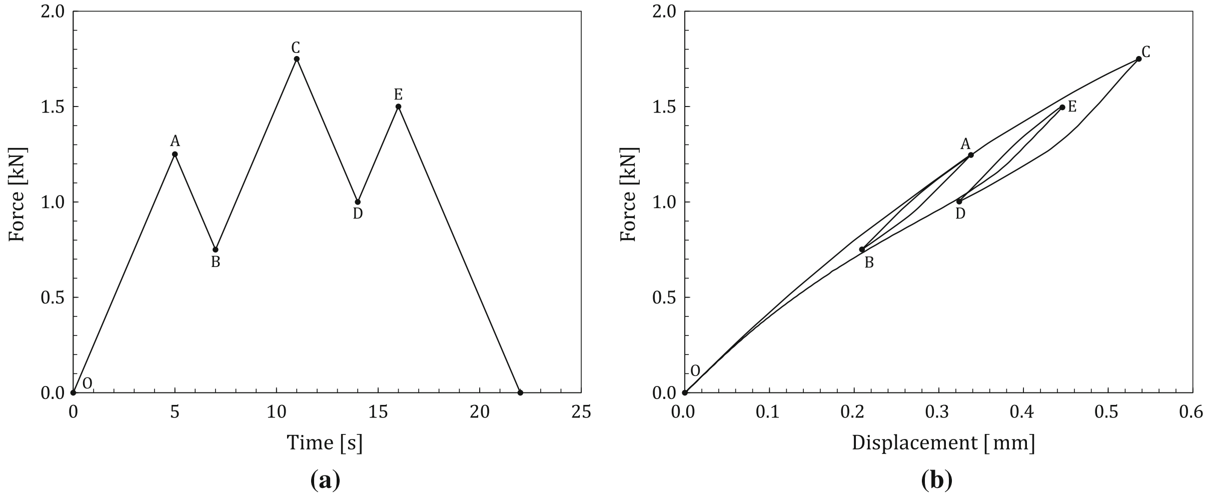

Fig. 10 Force–displacement curve of the top left corner point: **a** the loading path, **b** the numerical prediction by the FE simulation

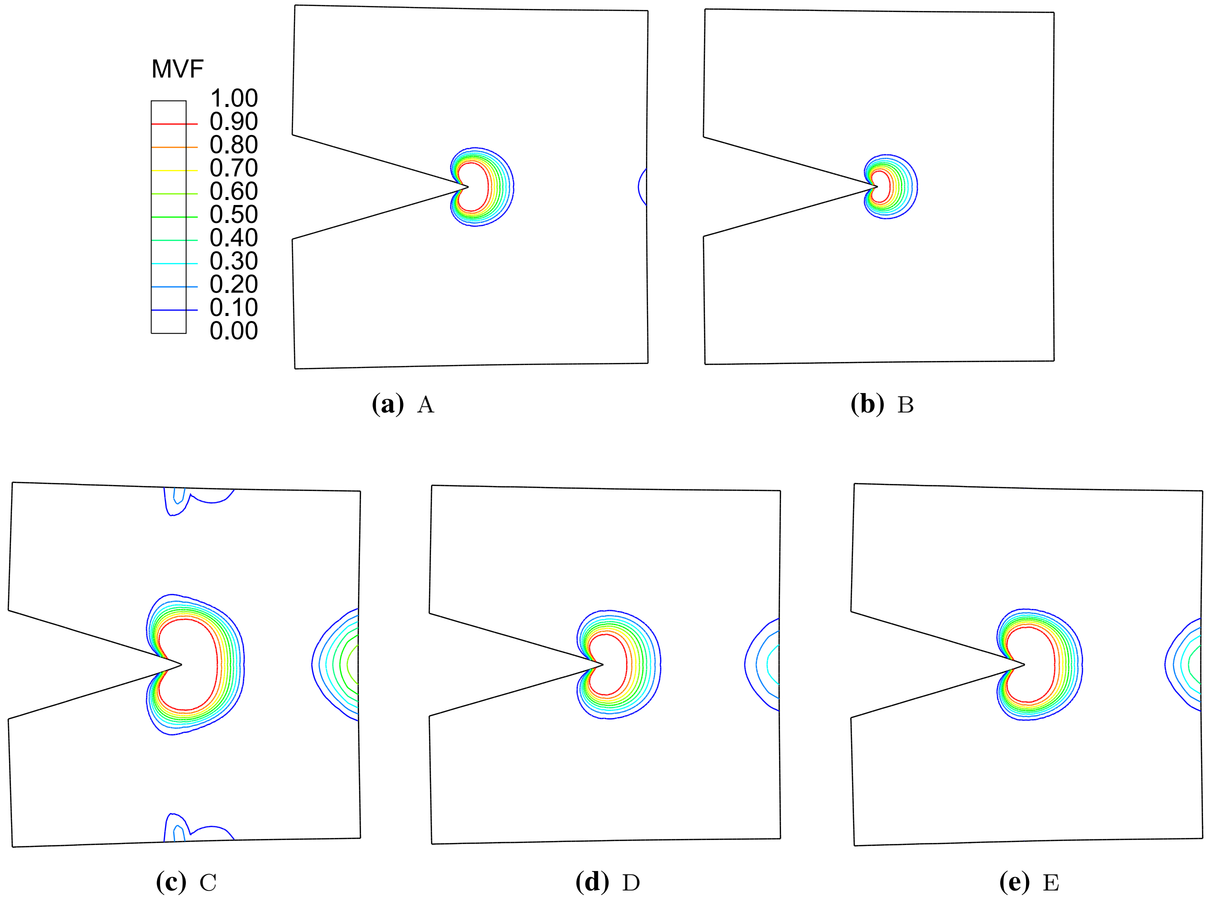

(a) A **(b)** B

(c) C **(d)** D **(e)** E

Fig. 11 Martensite volume fraction contour plots at different loading points

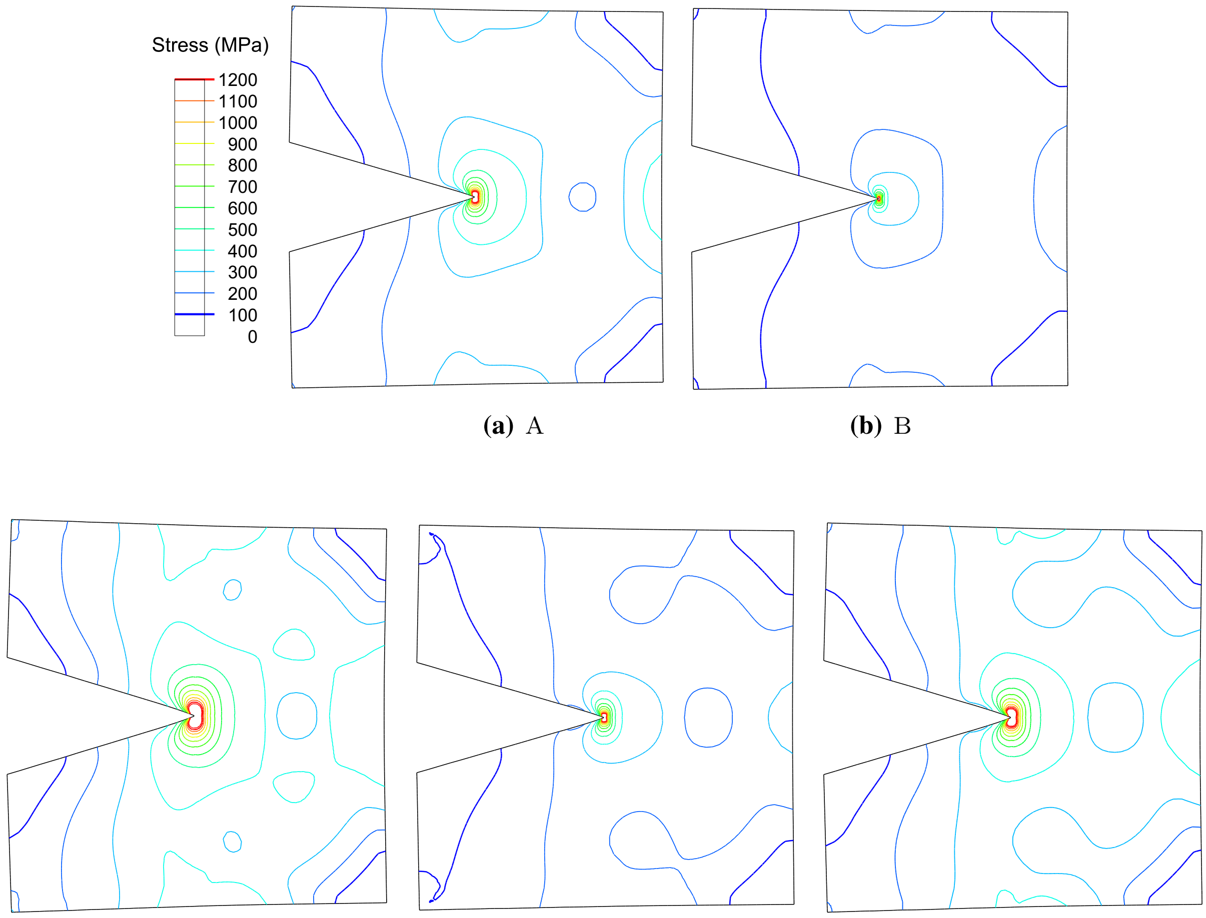

(a) A **(b)** B

(c) C **(d)** D **(e)** E

Fig. 12 Mises stress contour plots at different loading points

The red contour line near the crack tip indicates that the stress has exceeded 1200 MPa, while the material within this area has completely transformed to martensite. The blue contour line indicates the initiation of martensite phase transformation, and the corresponding transformation stress is around 400 MPa. With the partial unloading from A to B, stress level on the specimen shows an overall decrease and the region of stress concentration shrinks back. Phase transformation zone around the crack tip contracts, while the martensite at the right edge disappears. Then, at the maximum loading point C, phase transformation zone around the crack tip grows dramatically due to the expansion of the high-stress region, while partial phase transformation occurs at all edges. Subsequently, the unloading to D results in shrinkage of the phase transformation zone at the crack tip and right edge, and the disappearance of the phase transformation zone at the top and bottom edges. Finally, the incomplete loading from D to E again leads to a slight growth of the phase transformation zone. In general, the stress concentration at the crack tip is the crucial factor to initiate phase transformation, while evolution of the phase transformation zone in turn affects the stress distribution on the specimen, especially around the crack tip. It is well known that phase transformation is the physical origin of hysteresis effect in SMA. Thus, by combination of Figs. 10, 11 and 12, it might be concluded that the internal loops on the force–displacement curve are the consequence of the partial phase transformation on the SMA specimen, especially around the crack tip.

10 Conclusion

In this paper, we studied the internal hysteresis of pseudoelastic SMA subjected to incomplete phase transformation and developed a finite-strain thermomechanical model. The mode began with a four-tier decomposition of the deformation gradient into thermal dilation, rigid body rotation, elastic and transformation parts, which overcame the uniqueness problem of the intermediate stress-free configuration. Helmholtz free energy function comprised the reversible, irreversible thermodynamic processes and physical constraints of both. Based on the PVP, first and second laws of thermodynamics, we established a thermodynamic consistent framework, wherein the dissipation inequality and temperature evolution due to internal heat source were well discussed. Constitutive equations were derived from the Helmholtz free energy and established framework. A yield criterion considering the incomplete phase transformation was introduced, which separately described the forward internal hysteresis, the reverse internal hysteresis and the main hysteresis loops. Numerical implementation of the model includes the backward Euler discretization and the cutting-plane algorithm. The model was validated against the experimental data with various complex internal hysteresis loops, followed by a free vibration analysis of antagonistic SMA wires. Finally, we carried out a FE simulation of a SMA crack specimen under incomplete loading–unloading conditions. Simulation results well demonstrated the global internal hysteresis loops on the specimen, and the evolution of local phase transformation zone at the crack tip.

Funding This study was funded by National Natural Science Foundation of China (11802241).

Compliance with ethical standards

Conflict of interest The authors declare that they have no conflict of interest.

References

1. Wang, J., Moumni, Z., Zhang, W., Xu, Y., Zaki, W.: A 3D finite-strain-based constitutive model for shape memory alloys accounting for thermomechanical coupling and martensite reorientation. Smart Mater. Struct. (2017). https://doi.org/10.1088/1361-665X/aa6c17
2. Yu, C., Kang, G., Kan, Q.: A micromechanical constitutive model for grain size dependent thermo-mechanically coupled inelastic deformation of super-elastic NiTi shape memory alloy. Int. J. Plast. **105**, 99–127 (2018). https://doi.org/10.1016/j.ijplas.2018.02.005
3. Moumni, Z., Zhang, Y., Wang, J., Gu, X.: A global approach for the fatigue of shape memory alloys. Shape Memory Superelast. **4**, 385–401 (2018). https://doi.org/10.1007/s40830-018-00194-2
4. Dhala, S., Mishra, S., Tewari, A., Alankar, A.: Modeling of finite deformation of pseudoelastic NiTi shape memory alloy considering various inelasticity mechanisms. Int. J. Plast. **115**, 216–237 (2019). https://doi.org/10.1016/j.ijplas.2018.11.018
5. Birman, V.: Review of mechanics of shape memory alloy structures. Appl. Mech. Rev. **50**, 629–646 (1997)
6. Savi, M.A., Paiva, A.: Describing internal subloops due to incomplete phase transformations in shape memory alloys. Arch. Appl. Mech. **74**, 637–647 (2005). https://doi.org/10.1007/s00419-005-0385-6
7. Tang, C., Wang, T., Huang, W., Sun, L., Gao, X.: Temperature sensors based on the temperature memory effect in shape memory alloys to check minor over-heating. Sens. Actuators A **238**, 337–343 (2016). https://doi.org/10.1016/j.sna.2015.11.033
8. Dhanalakshmi, K.: Shape memory alloy wire for self-sensing servo actuation. Mech. Syst. Signal Process. **83**, 36–52 (2017). https://doi.org/10.1016/j.ymssp.2016.05.042
9. Formentini, M., Lenci, S.: An innovative building envelope (kinetic façade) with Shape Memory Alloys used as actuators and sensors. Autom. Constr. **85**, 220–231 (2018). https://doi.org/10.1016/j.autcon.2017.10.006
10. Rizzello, G., Mandolino, M.A., Schmidt, M., Naso, D., Seelecke, S.: An accurate dynamic model for polycrystalline shape memory alloy wire actuators and sensors. Smart Mater. Struct. **28**, 25020 (2019)
11. Tang, T., Felicelli, S.D.: Micromechanical investigations of polymer matrix composites with shape memory alloy reinforcement. Int. J. Eng. Sci. **94**, 181–194 (2015). https://doi.org/10.1016/j.ijengsci.2015.05.008
12. Song, S.-H., Lee, J.-Y., Rodrigue, H., Choi, I.-S., Kang, Y.J., Ahn, S.-H.: 35 Hz shape memory alloy actuator with bending-twisting mode. Sci. Rep. **6**, 21118 (2016). https://doi.org/10.1038/srep21118
13. Mohd Jani, J., Leary, M., Subic, A.: Designing shape memory alloy linear actuators: a review. J. Intell. Mater. Syst. Struct. **28**, 1699–1718 (2017). https://doi.org/10.1177/1045389X16679296
14. Huang, X., Kumar, K., Jawed, M.K., Mohammadi Nasab, A., Ye, Z., Shan, W., Majidi, C.: Highly dynamic shape memory alloy actuator for fast moving soft robots. Adv. Mater. Technol. **4**, 1800540 (2019). https://doi.org/10.1002/admt.201800540
15. Wang, J., Zhang, W., Zhu, J., Xu, Y., Gu, X., Moumni, Z.: Finite element simulation of thermomechanical training on functional stability of shape memory alloy wave spring actuator. J. Intell. Mater. Syst. Struct. **30**, 1239–1251 (2019). https://doi.org/10.1177/1045389X19831356
16. Xue, L., Dui, G., Liu, B., Xin, L.: A phenomenological constitutive model for functionally graded porous shape memory alloy. Int. J. Eng. Sci. **78**, 103–113 (2014). https://doi.org/10.1016/j.ijengsci.2014.02.013

17. Mohd Jani, J., Leary, M., Subic, A., Gibson, M.A.: A review of shape memory alloy research, applications and opportunities. Mater. Des. **56**, 1078–1113 (2014). https://doi.org/10.1016/j.matdes.2013.11.084
18. Qian, H., Li, H., Song, G.: Experimental investigations of building structure with a superelastic shape memory alloy friction damper subject to seismic loads. Smart Mater. Struct. **25**, 125026 (2016). https://doi.org/10.1088/0964-1726/25/12/125026
19. Dutta, S.C., Majumder, R.: Shape memory alloy (SMA) as a potential damper in structural vibration control. In: Advances in Manufacturing Engineering and Materials. Springer, pp. 485–492 (2019). https://doi.org/10.1007/978-3-319-99353-9_51
20. Bogue, R.: Shape-memory materials: a review of technology and applications. Assem. Autom. **29**, 214–219 (2009). https://doi.org/10.1108/01445150910972895
21. Zhang, Y., Moumni, Z., Zhu, J., Zhang, W.: Effect of the amplitude of the training stress on the fatigue lifetime of NiTi shape memory alloys. Scripta Mater. **149**, 66–69 (2018). https://doi.org/10.1016/j.scriptamat.2018.02.012
22. Abdullah, E., Gaikwad, P., Azid, N., Abdul Majid, D., Mohd Rafie, A.: Temperature and strain feedback control for shape memory alloy actuated composite plate. Sens. Actuators A **283**, 134–140 (2018). https://doi.org/10.1016/j.sna.2018.09.059
23. Spindler, C., Juhre, D.: Development of a shape memory alloy actuator using generative manufacturing. Int. J. Adv. Manuf. Technol. **97**, 4157–4166 (2018). https://doi.org/10.1007/s00170-018-2153-0
24. Tanaka, K., Nishimura, F., Tobushi, H.: Phenomenological Analysis on Subloops in Shape Memory Alloys Due to Incomplete Transformations. J. Intell. Mater. Syst. Struct. **5**, 487–493 (1994). https://doi.org/10.1177/1045389X9400500404
25. Lexcellent, C., Tobushi, H.: Internal loops in pseudoelastic behaviour of Ti–Ni shape memory alloys: experiment and modelling. Meccanica **30**, 459–466 (1995). https://doi.org/10.1007/BF01557078
26. Tobushi, H., Endo, M., Ikawa, T., Shimada, D.: Pseudoviscoelastic behavior of TiNi shape memory alloys under stress-controlled subloop loadings. Arch. Mech. **55**, 519–530 (2003)
27. Pieczyska, E.A., Tobushi, H., Nowacki, W.K., Gadaj, S.P., Sakuragi, T.: Subloop deformation behavior of TiNi shape memory alloy subjected to stress-controlled loadings. Mater. Trans. **48**, 2679–2686 (2007). https://doi.org/10.2320/matertrans.MRA2007097
28. Takeda, K., Tobushi, H., Miyamoto, K., Pieczyska, E.A.: Superelastic deformation of TiNi shape memory alloy subjected to various subloop loadings. Mater. Trans. **53**, 217–223 (2012). https://doi.org/10.2320/matertrans.M2011288
29. Rao, A., Ruimi, A., Srinivasa, A.R.: Internal loops in superelastic shape memory alloy wires under torsion: experiments and simulations/predictions. Int. J. Solids Struct. **51**, 4554–4571 (2014). https://doi.org/10.1016/j.ijsolstr.2014.09.002
30. Boyd, J., Lagoudas, D.: A thermodynamical constitutive model for shape memory materials. Part I. The monolithic shape memory alloy. Int. J. Plast **12**, 805–842 (1996). https://doi.org/10.1016/S0749-6419(96)00030-7
31. Bo, Z., Lagoudas, D.C.: Thermomechanical modeling of polycrystalline SMAs under cyclic loading, part IV: modeling of minor hysteresis loops. Int. J. Eng. Sci. **37**, 1205–1249 (1999). https://doi.org/10.1016/S0020-7225(98)00116-5
32. Ortin, J., Delaey, L.: Hysteresis in shape-memory alloys. Int. J. Non Linear Mech. **37**, 1275–1281 (2002). https://doi.org/10.1016/S0020-7462(02)00027-6
33. Matsuzaki, Y., Funami, K., Naito, H.: Inner loops of pseudoelastic hysteresis of shape memory alloys: Preisach approach, vol. 4699, pp. 355–364 (2002). https://doi.org/10.1117/12.474993
34. Ikeda, T., Nae, F.A., Naito, H., Matsuzaki, Y.: Constitutive model of shape memory alloys for unidirectional loading considering inner hysteresis loops. Smart Mater. Struct. **13**, 916–925 (2004). https://doi.org/10.1088/0964-1726/13/4/030
35. Bernardini, D., Pence, T.J.: Uniaxial modeling of multivariant shape-memory materials with internal sublooping using dissipation functions. Meccanica **40**, 339–364 (2005). https://doi.org/10.1007/s11012-005-2103-4
36. Kishore Kumar, M., Sakthivel, K., Sivakumar, S.M., Lakshmana Rao, C., Srinivasa, A.: Thermomechanical modeling of hysteresis in SMAs using the dissipationless reference response. Smart Mater. Struct. (2007). https://doi.org/10.1088/0964-1726/16/1/S04
37. Heintze, O., Seelecke, S.: A coupled thermomechanical model for shape memory alloys-From single crystal to polycrystal. Mater. Sci. Eng. A **481–482**, 389–394 (2008). https://doi.org/10.1016/j.msea.2007.08.028
38. Müller, I.: Pseudo-elastic hysteresis in shape memory alloys. Phys. B **407**, 1314–1315 (2012). https://doi.org/10.1016/j.physb.2011.06.088
39. Viet, N.V., Zaki, W., Umer, R., Xu, Y.: Mathematical model for superelastic shape memory alloy springs with large spring index. Int. J. Solids Struct. **185**, 159–169 (2020)
40. Scalet, G., Niccoli, F., Garion, C., Chiggiato, P., Maletta, C., Auricchio, F.: A three-dimensional phenomenological model for shape memory alloys including two-way shape memory effect and plasticity. Mech. Mater. **136**, 103085 (2019)
41. Müller, C., Bruhns, O.T.: A thermodynamic finite-strain model for pseudoelastic shape memory alloys. Int. J. Plast. **22**, 1658–1682 (2006). https://doi.org/10.1016/j.ijplas.2006.02.010
42. Teeriaho, J.P.: An extension of a shape memory alloy model for large deformations based on an exactly integrable Eulerian rate formulation with changing elastic properties. Int. J. Plast. **43**, 153–176 (2013). https://doi.org/10.1016/j.ijplas.2012.11.009
43. Xiao, H.: An explicit, straightforward approach to modeling SMA pseudoelastic hysteresis. Int. J. Plast. **53**, 228–240 (2014). https://doi.org/10.1016/j.ijplas.2013.08.010
44. Reese, S., Christ, D.: Finite deformation pseudo-elasticity of shape memory alloys: constitutive modelling and finite element implementation. Int. J. Plast. **24**, 455–482 (2008). https://doi.org/10.1016/j.ijplas.2007.05.005
45. Arghavani, J., Auricchio, F., Naghdabadi, R.: A finite strain kinematic hardening constitutive model based on Hencky strain: general framework, solution algorithm and application to shape memory alloys. Int. J. Plast. **27**, 940–961 (2011). https://doi.org/10.1016/j.ijplas.2010.10.006

46. Paranjape, H.M., Manchiraju, S., Anderson, P.M.: A phase field: finite element approach to model the interaction between phase transformations and plasticity in shape memory alloys. Int. J. Plast. **80**, 1–18 (2016). https://doi.org/10.1016/j.ijplas.2015.12.007
47. Wang, J., Moumni, Z., Zhang, W., Zaki, W.: A thermomechanically coupled finite deformation constitutive model for shape memory alloys based on Hencky strain. Int. J. Eng. Sci. **117**, 51–77 (2017). https://doi.org/10.1016/j.ijengsci.2017.05.003
48. Dunne, F., Petrinic, N.: Introduction to Computational Plasticity. Oxford University Press, New York (2005)
49. Anand, L., Ames, N.M., Srivastava, V., Chester, S.A.: A thermo-mechanically coupled theory for large deformations of amorphous polymers. Part I: formulation. Int. J. Plast. **25**, 1474–1494 (2009). https://doi.org/10.1016/j.ijplas.2008.11.004
50. Wang, J., Moumni, Z., Zhang, W.: A thermomechanically coupled finite-strain constitutive model for cyclic pseudoelasticity of polycrystalline shape memory alloys. Int. J. Plast. **97**, 194–221 (2017). https://doi.org/10.1016/j.ijplas.2017.06.003
51. Qidwai, M.A., Lagoudas, D.C.: On thermomechanics and transformation surfaces of polycrystalline NiTi shape memory alloy material. Int. J. Plast. **16**, 1309–1343 (2000). https://doi.org/10.1016/S0749-6419(00)00012-7
52. Lagoudas, D., Hartl, D., Chemisky, Y., Machado, L., Popov, P.: Constitutive model for the numerical analysis of phase transformation in polycrystalline shape memory alloys. Int. J. Plast. **32–33**, 155–183 (2012). https://doi.org/10.1016/j.ijplas.2011.10.009